Science Arts & Métiers (SAM)

is an open access repository that collects the work of Arts et Métiers Institute of Technology researchers and makes it freely available over the web where possible.

To cite this version :

Influence of freestream turbulence on the flow over a wall roughness

M. A. Bucci [1,3] S. Cherubini,[2] J.-Ch. Loiseau [1] and J.-Ch. Robinet[1,*]

[1]*DynFluid, Arts et Métiers ParisTech, 151 Boulevard de l'Hopital, 75013 Paris, France*
[2]*Department of Mechanics, Mathematics, and Management, Politecnico di Bari,
via Re David 200, 70100 Bari, Italy*
[3]*TAU, Inria, Université Paris-Saclay, CNRS, LISN, Orsay, France*

The effect of freestream turbulence on the dynamics of an incompressible flow past a cylindrical roughness element in subcritical conditions (i.e., for Reynolds numbers below the onset of linear instability) has been investigated by the joint application of direct numerical simulations, linear modal and nonmodal stability analyses, and dynamic mode decomposition. At first, the influence of the Reynolds number and the ratio of the boundary layer's thickness to roughness height on the three-dimensional spatiotemporal (global) stability of the flow has been investigated. Depending on the operating conditions, the leading instability can either be varicose (symmetric) or sinuous (antisymmetric). In both cases, when the flow is excited by broadband frequency forcing, dynamic mode decomposition extracts only varicose coherent structures even though optimal response analysis predicts a strong amplification of sinuous disturbances having frequency close to that of the marginally stable sinuous eigenmode. This apparent discrepancy is attributed to the fact that the sinuous instability is sensitive to a very limited range of frequencies barely excited by freestream turbulence while varicose disturbances are associated with high amplification in a much wider frequency range. Hence, in this case the flow behaves as an amplifier of varicose perturbations rather than a resonator. Consequences on the subsequent transition to turbulence have been studied, highlighting that varicose perturbations extract energy from the near-wake region, get continuously amplified due to the excitation provided by freestream turbulence, and eventually give rise to a shedding of hairpin vortices.

I. INTRODUCTION

Understanding and predicting the laminar-turbulent transition in boundary layer flows has been a long-standing challenge for fluid dynamicists, in particular due to its high sensitivity on the environmental conditions. A phenomenological description of the various routes transition could take, depending mostly on the presence of external disturbances or freestream turbulence, has been proposed in Refs. [1,2]. In addition to the external environmental conditions, transition is also strongly affected by the features of the wall itself such as compliancy [3], porosity [4,5], or the presence of microscopic [6] or finite-size roughness elements [7–10]. While it is known that spanwise-invariant roughness elements promote transition [7], three-dimensional elements have more subtle and intricate effects on the stability properties of the flow. When impinging on such roughness element, the spanwise vorticity of the upstream boundary layer wraps around it, creating horseshoe vortices [11] whose characteristics and number depend essentially on the geometrical
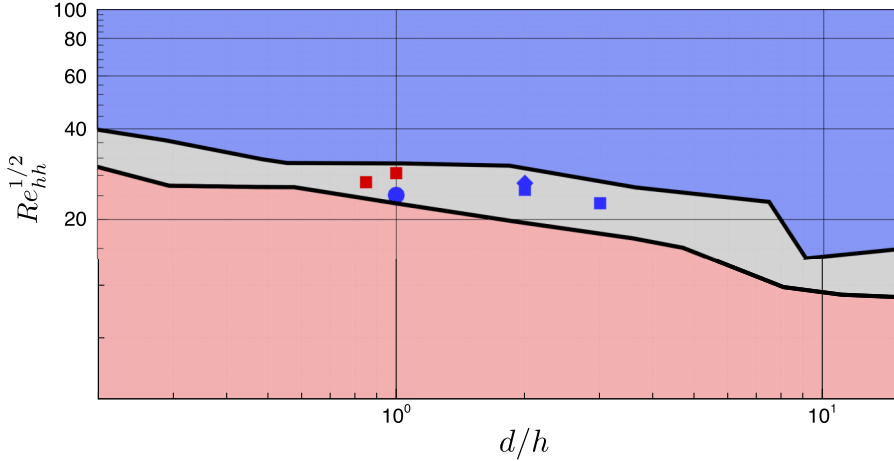
FIG. 1. Reproduction of the von Doenhoff–Braslow diagram, representing the *transition region* (gray region between the solid lines) and the steady (red zone below the bottom line) and the turbulent regions (blue zone above the top line), depending on the aspect ratio of the roughness element and the roughness Reynolds number Re_{hh}. The different symbols report the critical Reynolds numbers computed using three-dimensional global stability analysis: ■ for the cylinder [9], ● for the hemisphere [10], ♦ for the bump [43]. Red symbols indicate sinuous unstable global modes; blues ones denote varicose instability.

properties of the roughness element itself [12]. Further downstream, the legs of these horseshoe vortices become streamwise-oriented vortices which, due to the lift-up effect [13], give rise to velocity streaks [14]. The streamwise evolution of these roughness-induced streaks has been studied by various authors [15–20]. For supersonic and hypersonic boundary layers, it has been observed that long-lived streamwise streaks can support instability modes that did not exist in the absence of the roughness element [21–23]. In general, roughness elements having a symmetric (asymmetric) shape have been found to support a dominant convective instability mode symmetrically (asymmetrically) distributed around the wake centerline [21]. Antisymmetric instabilities have been reported as well, for sufficiently tall cylindrical roughness elements [24,25]. Based on many of these experimental and numerical studies, it was found that the maximum energy growth scales as the square of the so-called roughness Reynolds number

$$\mathrm{Re}_{hh} = \frac{U_{BL}(h)h}{\nu}$$

with h being the height of the roughness element, $U_{BL}(h)$ the would-be value of the Blasius velocity profile at this particular height, and ν the kinematic velocity of the fluid considered. Many authors have studied the transient growth and breakdown of streaks under freestream vortical disturbances or turbulence [26–29]. However, the presence of the roughness element induces the formation of a separation region, whose influence on the stability of the flow is still open to debate and appears to depend on a large number of external parameters. In several flow conditions [8,30] unsteadiness is found to occur right downstream of the roughness element, where the separated zone may act as a *wave maker* [31].

Roughness-induced transition to turbulence was extensively studied during the 1950s [32]. Given this body of literature, in Ref. [33] has been published a diagram correlating the roughness element's aspect ratio $\eta = d/h$ (with d being the roughness element's equivalent diameter) with the roughness Reynolds number at which transition was reported. A reproduction of this diagram can be seen in Fig. 1. Based on these results, the empirical relation $\mathrm{Re}_{hh}^c \propto 600\eta^{-2/5}$ has been proposed [33] to predict the onset of turbulence, where Re_{hh}^c is the critical roughness Reynolds number. Despite the qualitative agreement between this empirical relation and the data reported in Ref. [33], it can be

seen that, for a given aspect ratio η, transition to turbulence may occur over a relatively wide range of roughness Reynolds numbers as reported in various experimental works [34,35].

In an attempt to provide a physical explanation for the onset of unsteadiness and its dependency on the roughness element's geometrical properties, Refs. [20,36,37] have relied on a parallel flow assumption to conduct local stability analysis of the flow in various crossflow planes downstream of the roughness element. These local stability analyses (which can be either spatial or temporal) are based on the simplifying hypotheses that the perturbation is sinusoidal in the streamwise direction and that the three-dimensional base flow computed via direct numerical simulations is slightly changing in the same direction. In all cases, several locally unstable sinuous and varicose modes were found. Close to the separation bubble just behind the roughness element, the local unstable modes can be associated with an absolute instability [31], which in some cases may correspond to the main oscillation frequency recovered in the unsteady dynamics. It should be emphasized however that, despite its computational tractability, local stability of the flow in various crossflow planes suffers from two major drawbacks:

(1) the connection between these locally convective unstable modes far from the separation bubble and the fully three-dimensional coherent structures observed in the flow is still unclear to the present day;

(2) the necessity to rely on a parallel flow assumption does not allow us to be confident about such approach in the near-wake region where hairpin vortices actually originate from [17,38].

As a consequence, local stability analyses have been extended to the parabolized stability equation (PSE) framework [25,39,40], which does not rely on the parallel flow assumption. The agreement of the PSE results with numerical simulations in many cases has proven to be excellent. Although most of these studies have been performed for compressible flows, literature results have demonstrated that the roughness-induced transition mechanisms are similar across the speed regime [41,42]. However, thanks to the increased computational capabilities, researchers have recently been able to tackle the stability analysis of the Navier-Stokes operator linearized around the fully three-dimensional steady flow generated in the presence of the roughness element. These *global* stability analyses do not rely on any simplifying hypothesis on the perturbation shape and/or on the base flow, yielding an accurate estimate of the spatiotemporal asymptotic growth of small-amplitude disturbances on the selected base flow. In Ref. [9] the stability of the boundary layer flow in the presence of a cylindrical roughness element has been investigated, with particular attention to the influence of its aspect ratio. Successive works have tackled the global stability of the flow behind a hemispherical protuberance [10] and a smooth bump [43]. In all these cases, the critical Reynolds numbers predicted by such fully three-dimensional linear stability analysis, Re_c, have proven to be consistent with the upper band of the transition region in the von Doenhoff–Braslow diagram (see Fig. 1), thus suggesting that a fully three-dimensional global instability analysis can provide an accurate estimate for this upper threshold.

Additionally, for cylindrical elements, in Ref. [9] it has been found that the flow could sustain two different global instabilities, a sinuous one (similar to the von Kármán vortex street) and a varicose one (associated with the creation of hairpin vortices in the nonlinear stage). The selection of the dominant instability is governed by the aspect ratio of the roughness element, thinner elements being prone to a sinuous instability while large ones exhibit varicose oscillations in the near wake. These theoretical predictions have recently been experimentally confirmed [44]. However, these experimental observations have indicated that transition may occur also at lower values than that of the critical Reynolds number Re_c, albeit following different dynamics.

Despite a number of numerical [39], theoretical [45], and experimental [46] studies on this subject, it is still unclear which physical mechanisms may cause the subcritical transition to turbulence close to the lower limit of the transition diagram (see Fig. 1). Considering once again a cylindrical roughness element, in Ref. [47] some preliminary explanation has been attempted for this subcritical transition using insights from pseudospectrum analysis. It was found that exciting the most sensitive varicose eigenmode of the linearized Navier-Stokes operator, whose frequency closely matches that measured experimentally, allows the growth of disturbances at the same frequency by up to six

orders of magnitude. In that particular operating condition, the transition to unsteadiness reported experimentally appeared to result from a quasiresonance of the leading varicose eigenmode due to external forcing rather than purely from the non-normality of the linearized Navier-Stokes operator as classically supposed. Although the flow is strongly non-normal, the amplification of the external forcing at a given frequency mostly results from the resonance of a single eigenmode, though other eigenmodes can also contribute to the response, albeit to a lesser extent. However, Ref. [47] tackled a very few flow cases, all characterized by a leading varicose eigenmode only, the sinuous mode being either very stable or even absent from the converged part of the eigenspectrum. Hence, the sensitivity of the sinuous eigenmode, as well as the influence of the Reynolds number and of the boundary-layer thickness of the incoming flow on the properties (frequency, symmetry) of the most unstable and/or sensitive modes of the spectrum, remains to be investigated. Changing these flow parameters can substantially modify the dynamics of the flow, which might no longer behave as a resonator as in Ref. [47] but rather as an amplifier of a broadband range of frequencies [48], as already observed for very small roughness elements [30,49]. This work aims at investigating these points with the joint application of direct numerical simulation (DNS) and dynamic mode decomposition, for unraveling the dynamics of the boundary layer flow past a cylindrical roughness element subject to freestream turbulence. The origin of the flow structures extracted from DNS by dynamic mode decomposition will be explained using modal and nonmodal linear stability and sensitivity analyses, which have proven efficient to capture convective flow instabilities in a global framework [48,50]. This analysis will be a useful tool for investigating the influence of the Reynolds number and of the boundary-layer thickness of the incoming flow on the flow stability.

The paper is structured as follows: Section II presents the flow configuration and the numerical methods for direct numerical simulations, dynamic mode decomposition, global stability, and optimal forcing analysis. A parametric analysis is provided in Sec. III using linear stability tools. In Sec. IV, dynamic mode decomposition as well as optimal forcing and perturbation analyses provide insights into the dynamics of the flow in different operating conditions, whereas the transition scenario is discussed in Sec. V. Finally, concluding remarks and perspectives are given in Sec. VI.

II. FLOW CONFIGURATION AND NUMERICAL METHODS

A. Flow configuration and governing equations

The boundary layer flow impinging on a wall-mounted cylindrical roughness element of diameter d and height h is studied numerically. Throughout this work, the aspect ratio $\eta = d/h$ is fixed to unity. A schematic representation of the domain considered herein is depicted in Fig. 2. The roughness element is centered at $(x, z) = (0, 0)$. The numerical domain extends from $x = -25$ to $x = 90$ in the streamwise direction, $y = 0$ to $y = 40$ in the wall-normal direction, and $z = -5$ to $z = 5$ in the spanwise one. It should be noted that although periodic boundary conditions are imposed in the spanwise direction, the extent of the computational domain in this direction is sufficient in order to ensure that the roughness element behaves as being isolated [51,52].

The flow is assumed to be incompressible and the fluid to be Newtonian so that its dynamics are governed by the following Navier-Stokes equations,

$$\frac{\partial \boldsymbol{U}}{\partial t} + \boldsymbol{\nabla} \cdot (\boldsymbol{U} \otimes \boldsymbol{U}) = -\boldsymbol{\nabla} P + \frac{1}{\mathrm{Re}} \nabla^2 \boldsymbol{U},$$

$$\boldsymbol{\nabla} \cdot \boldsymbol{U} = 0,$$

where $\boldsymbol{U} = (U, V, W)^T$ is the velocity vector and P is the pressure field. The Reynolds number is defined as

$$\mathrm{Re} = \frac{U_\infty h}{\nu},$$

with U_∞ being the velocity in the freestream, h the height of the roughness element, and ν the kinematic viscosity of the working fluid. The precise flow configuration is also characterized by a
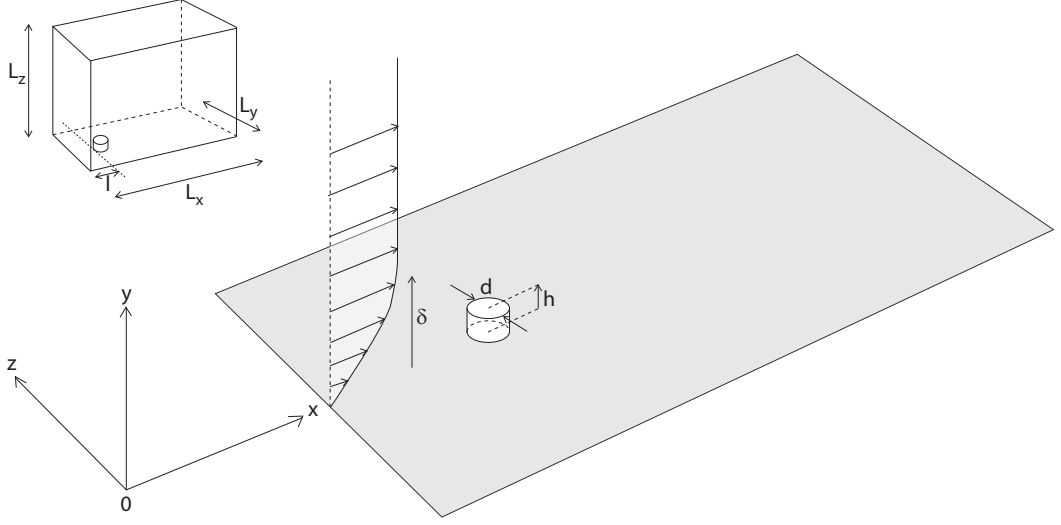
FIG. 2. Sketch of the flow case studied.

second nondimensional parameter, hereafter called the *shear ratio* and defined as h/δ^*, where δ^* is the displacement thickness of the boundary layer in the absence of the roughness element at its location. This second parameter thus characterizes how immersed the roughness element is in the boundary layer. Differently from the roughness Reynolds number, classically used for evaluating the transition threshold of the considered flow, this parameter accounts not only for the velocity, but also for the shear of the flow hitting the head of the roughness element, which may considerably affect stability and transition to turbulence. All of the configurations considered herein are summarized in Table I.

As stated before, periodic boundary conditions are prescribed in the spanwise direction while a no-slip boundary condition is imposed at the wall. A Neumann boundary condition is used at the upper boundary of the computational domain. Regarding the inflow and outflow boundary conditions, these change depending on the analysis conducted and will be stated whenever needed in the next subsections. The Navier-Stokes equations are solved using the incompressible flow solver

TABLE I. Summary of the flow parameters for all of the flow cases considered herein. For all of them, the aspect ratio η of the roughness element is fixed to unity. The two configurations on which Secs. IV and V focus are highlighted in bold. ST (resp. UN) refers to steady (resp. unsteady) flow, while S (resp. V) refers to the sinuous (resp. varicose) symmetry of the leading eigenmode.

Re	Re_{hh}	h/δ^*	ST/UN	S/V
700	526	1.47	ST	
700	582	1.70	ST	
700	**639**	**2.04**	ST	V
700	683	2.56	UN	V
900	675	1.47	ST	V
900	821	2.04	UN	S
1000	**750**	**1.47**	ST	S
1200	900	1.47	UN	S
1200	997	1.70	UN	S
1200	1095	2.04	UN	S

NEK5000 [53] which is based on the spectral element method [54,55]. A $\mathbb{P}_N - \mathbb{P}_{N-2}$ formulation has been used: the velocity field is discretized using Nth degree Lagrange interpolants, defined on the Gauss-Lobatto-Legendre quadrature points, as basis and trial functions, while the pressure field is discretized using Lagrange interpolants of degree $N-2$ defined on the Gauss-Legendre quadrature points. All results presented hereafter are based on the polynomial degree $N = 8$ (a grid convergence study for similar flow configurations has been provided in [47]). Finally, time integration is performed using the BDF3/EXT3 scheme: integration of the viscous terms relies on backward differentiation (BDF3), while the convective terms are integrated explicitly using a third order accurate extrapolation (EXT3).

B. Synthetic freestream turbulence

A well established method to mimic grid turbulence in boundary layer flow numerically is to use a sum of eigenmodes from the continuous branch of the Orr-Sommerfeld-Squire (OSS) operator [2,56]. This method allows us to introduce a perturbation in the numerical experiment which naturally penetrates in the boundary layer [56] without triggering synthetic resonant mechanisms [57] which can potentially lead to a biased laminar-to-turbulent transition. Once the streamwise, spanwise, and wall-normal wave numbers have been defined (resp. α, β, and γ), as well as the Reynolds number, the eigenvalues of the OSS operator can be obtained analytically. For a given triplet (α, β, γ), the corresponding one-dimensional eigenmode $\hat{\boldsymbol{u}}(y)$ has to obey the no-slip boundary condition and will be modulated in the wall-normal direction with wave number γ and constant amplitude. Invoking Taylor's hypothesis, the streamwise wave number α can be replaced by the frequency $\omega = \alpha U_\infty$ such that the eigenmode associated with the kth wave number triplet is given by

$$\boldsymbol{u}_k(y, z, t) = \hat{\boldsymbol{u}}(y)e^{i(\beta z - \omega t)},$$

where $\hat{\boldsymbol{u}}(y)$ implicitly depends on the chosen value of γ. Assuming that each of these eigenmodes is normalized such that it has unit norm, the perturbation's velocity profile $\boldsymbol{u}$ to be added at the inflow of the computational domain is given by

$$\boldsymbol{u}(y, z, t) = \sum_{k=k_l}^{k_u} A_k \boldsymbol{u}_k(y, z, t),$$

where A is the amplitude associated with each eigenmode. These amplitudes are sampled from a distribution ensuring that the desired turbulent energy spectrum is prescribed at the inflow. In the present work, this spectrum is chosen to be the von Kármán spectrum

$$E(k) = \frac{2}{3} \frac{a(kL)^4}{[b + (kL)^2]^{17/6}} Lq,$$

where L is the integral length scale and q the turbulent kinetic energy. The two constants in the above spectrum are chosen as $a = 1.606$ and $b = 1.350$. Once the minimum k_l and maximum k_u are fixed depending on the numerical resolution, the energy is distributed over 20 k shells. Each of these is homogeneously divided in 20 triads of (ω, β, γ) values defining the vertices of a dodecahedron inscribed in the given k shell. Defining the turbulence intensity

$$\text{Tu} = \sqrt{\frac{u_{\text{rms}}^2 + v_{\text{rms}}^2 + w_{\text{rms}}^2}{3}},$$

the expression of the turbulent energy spectrum can be rewritten as

$$E(k) = \frac{a(kL)^4}{[b + (kL)^2]^{17/6}} L\,\text{Tu}^2.$$

Given a predefined numerical resolution, the only parameters left to properly define the characteristics of the desired freestream turbulence are thus the integral length scale L and the turbulent intensity Tu. Note that due to the stable nature of the modes on the continuous branch of the OSS spectrum, the freestream turbulence has to decay exponentially. For a prescribed turbulent intensity Tu = 0.18%, unsteadiness is triggered by the imposed freestream turbulence and an exponential decay of the turbulence intensity can be observed (see the validation in Appendix B). At a distance from the wall equal to 30, the intensity of freestream turbulence in the streamwise direction follows the decay law

$$\text{Tu} \propto (x + x_0)^{-n}$$

with $n \approx 0.71$ as also suggested in Ref. [56].

C. Dynamic mode decomposition

The dynamics of the flow excited by freestream turbulence is then analyzed to unveil the spectral features of the system. In this work, spatiotemporal coherent structures are extracted from direct numerical simulation using the dynamic mode decomposition (DMD) method proposed in Ref. [58]. Given a sequence $\{\boldsymbol{u}(\boldsymbol{x}, t_k)\}$ for $k = 1, \ldots, n$ of evenly sampled velocity snapshots, DMD aims to find the best low-rank linear operator A solution of the following minimization problem,

$$\text{minimize}_A \sum_{i=1}^{n-1} \|\boldsymbol{u}_{i+1} - A\boldsymbol{u}_i\|_2^2 \ \text{ subject to rank } A = r, \tag{1}$$

where A is known as the DMD operator. A suboptimal yet tractable solution to this rank-constrained minimization problem has been proposed in Ref. [58]. Given the data matrices

$$X = [\boldsymbol{u}_1 \quad \boldsymbol{u}_2 \quad \cdots \quad \boldsymbol{u}_{n-1}]$$

and the time-shifted counterpart

$$Y = [\boldsymbol{u}_2 \quad \boldsymbol{u}_3 \quad \cdots \quad \boldsymbol{u}_n],$$

a low-dimensional approximation of the DMD operator can be constructed as follows,

$$U_X^T A U_X = U_X^T Y V_X \Sigma_X^{-1},$$

where $U_X \Sigma_X V_X^T$ is the truncated singular value decomposition of the data matrix X. The low-dimensional DMD operator $S = U_X^T A U_X$ is an $r \times r$ matrix whose eigenvalues μ_S are reasonable approximations of the true eigenvalues μ_A of A. Additionally, approximation of the eigenvectors $\boldsymbol{\Phi}$ of A can be obtained as

$$\boldsymbol{\Phi} \approx U\boldsymbol{\Gamma},$$

where $\boldsymbol{\Gamma}$ are the eigenvectors of S. Finally, the growth rate σ and circular frequency ω associated with each DMD mode can be recovered by

$$\sigma + i\omega = \frac{\log(\mu_S)}{\Delta T},$$

where ΔT is the sampling period between two consecutive snapshots.

Once the low-dimensional DMD operator S has been identified from data, it is possible to expand the time evolution of the corresponding reduced-order model $\boldsymbol{q}_k = S^k \boldsymbol{q}_0$ (with $\boldsymbol{q} \in \mathbb{R}^r$ the state vector of the reduced-order model and $\boldsymbol{q}_0$ the initial condition) in terms of the DMD modes [59]. Given the eigendecomposition

$$S = \boldsymbol{\Gamma} D_\mu Z,$$

with Γ (resp. Z) being the right (resp. left) eigenvectors of S and D_μ the diagonal matrix containing its eigenvalues, the expansion of the dynamics thus reads

$$q_k = \Gamma D_\mu^k Z q_0 = \sum_{i=1}^{r} \gamma_i \mu_i^k z_i^H q_0 = \sum_{i=1}^{r} \gamma_i \mu_i^k \alpha_i, \tag{2}$$

where γ_i (resp. z_i) is the ith right (resp. left) eigenvector of S and $\alpha_i = z_i^H q_0$ is the projection of the initial condition onto the ith left eigenvector. This weight α_i thus represents the contribution of the ith DMD mode to the initial condition, allowing us to rank them.

For more details about DMD and its connection to the Koopman operator [60], interested readers are referred to the recent book Ref. [61].

D. Linear stability

Investigating the global stability of the system is a mandatory step for uncovering the existence of supercritical bifurcations and finding stable global modes which can be possible candidates for quasiresonance mechanisms such as that discussed in Ref. [47]. Let us consider infinitesimal perturbations u evolving in the vicinity of a steady solution of the Navier-Stokes equations U_b, which is computed via direct numerical simulations of the flow over a roughness element mounted on a flat plate. The dynamics of perturbations of the given base flow is governed by the linearized Navier-Stokes equations

$$\frac{\partial u}{\partial t} + (u \cdot \nabla)U_b + (U_b \cdot \nabla)u = -\nabla p + \frac{1}{\text{Re}} \nabla^2 u,$$

$$\nabla \cdot u = 0, \tag{3}$$

their adjoint counterparts being

$$\frac{\partial u^\dagger}{\partial t} + (\nabla U_b)^T u^\dagger + (U_b \cdot \nabla)u^\dagger = -\nabla p^\dagger + \frac{1}{\text{Re}} \nabla^2 u^\dagger,$$

$$\nabla \cdot u^\dagger = 0. \tag{4}$$

Once projected onto a divergence-free vector space, the linearized Navier-Stokes equations can be compactly written as

$$\frac{\partial u}{\partial t} = Au \tag{5}$$

with A the projection of the linearized Navier-Stokes operator onto the divergence-free vector space. The asymptotic time evolution of an infinitesimal perturbation u is then governed by the eigenspectrum of A. Due to the very large dimensions of A after discretization of the linearized Navier-Stokes equations, its leading eigenvalues cannot be easily obtained using direct eigenvalue solvers. For this reason, we use a time-stepper approach [62,63], which computes approximations of the leading eigenpairs of the exponential propagator

$$M(\Delta t) = e^{A \Delta t},$$

whose action onto an initial vector is easily obtained by time-marching the linearized Navier-Stokes equations from $t = 0$ to $t = \Delta t$. Iterative eigenvalue solvers can then be used to project the propagator M onto an orthonormal set of vectors spanning a Krylov subspace of dimension k, hence resulting in a low-dimensional $k \times k$ Hessenberg matrix H. The eigenvalues $\lambda_k = \sigma_k + i\omega_k$ of H and their associated eigenvectors $\hat{u}$ provide a good approximation to those of M. In this work, an in-house Krylov-Schur algorithm [64,65] with a Krylov subspace dimension $k = 500$ and a sampling period $\Delta t = 0.748$ has been used.

In order to compute the equilibrium solution of the three-dimensional Navier-Stokes equations in the presence of the roughness element, a Blasius profile has been imposed at the inlet, chosen by

requiring that in the absence of the roughness element the flow would have the desired value of shear ratio. At the outlet points, an outflow boundary conditions has been imposed. In most of the flow cases considered here, the base flows have simply been computed by time-marching the Navier-Stokes equations until the norm of the residual drops below a given tolerance ($\|\partial \boldsymbol{u}/\partial t\| \leqslant 10^{-8}$), due to their linearly stable nature. Concerning the globally unstable cases, the BoostConv algorithm recently introduced in Ref. [66] has been used. For the linearized Navier-Stokes equations, a zero perturbation condition has been imposed at the inlet, together with a Neumann boundary condition at the outlet of the computational domain.

E. Optimal forcing

Optimal forcing analysis, also known as *resolvent analysis*, aims to determine the spatial support of the harmonic forcing able to induce the largest possible response in terms of kinetic energy. To tackle this problem, a forcing is introduced in the linearized Navier-Stokes equations such that

$$\frac{\partial \boldsymbol{u}}{\partial t} = A\boldsymbol{u} + \boldsymbol{f}. \tag{6}$$

Assuming a periodic forcing

$$\boldsymbol{f}(\boldsymbol{x}, t) = \hat{\boldsymbol{f}}(\boldsymbol{x}, \omega)e^{i\omega t} + \text{c.c.},$$

the response of the system takes the form

$$\boldsymbol{u}(\boldsymbol{x}, t) = \hat{\boldsymbol{u}}(\boldsymbol{x}, \omega)e^{i\omega t} + \text{c.c.}$$

Using this ansatz, the relation between $\hat{\boldsymbol{f}}$ and $\hat{\boldsymbol{u}}$ is given by

$$\hat{\boldsymbol{u}} = (i\omega\mathbf{I} - \mathbf{A})^{-1}\hat{\boldsymbol{f}}, \tag{7}$$

where the resolvent operator $\boldsymbol{R}(\omega) = (i\omega\mathbf{I} - \mathbf{A})^{-1}$ has the role of a transfer function between the harmonic forcing $\hat{\boldsymbol{f}}$ and the asymptotic response $\hat{\boldsymbol{u}}$. In order to find the forcing field at a given frequency ω that maximizes the response of the system, the quantity

$$\mathcal{R}(\omega) = \max_{f} \frac{\|(i\omega\mathbf{I} - \mathbf{A})^{-1}\boldsymbol{f}\|}{\|\boldsymbol{f}\|} = \|(i\omega\mathbf{I} - \mathbf{A})^{-1}\| \tag{8}$$

has to be optimized. The solution to this optimization problem is found iteratively by a direct-adjoint loop [67] which has been implemented in the NEK5000 code. More details on the algorithm are provided in Appendix A.

Concerning the boundary conditions, a zero-velocity condition has been prescribed at both the inflow and outflow, together with fringe regions aimed at killing the direct (adjoint) perturbation once it reaches the outflow (inflow). The streamwise extent of the domain and the characteristics of the fringe regions have been chosen so as to slightly affect the optimal forcing results, as also discussed in Ref. [47].

III. PARAMETRIC STUDY

In this section, the influence of the shear ratio and of the Reynolds number on the flow stability is studied, in order to select representative flow cases whose transition to turbulence will be analyzed in detail. Stability analyses of the three-dimensional steady states have been carried out for the parameters reported in Table I. The top panels of Fig. 3 provide three eigenspectra for Re = 700 and decreasing shear ratio (from left to right). For the highest considered value of the shear ratio, $h/\delta^* = 2.56$, the spectrum in the top left panel has two isolated modes, an unstable varicose one and a stable sinuous one, as well as a whole branch of linearly stable varicose modes. Decreasing the value of h/δ^*, the velocity gradients in the spanwise direction as well as the amplitudes of the streaks decrease, inducing at first a stabilization of the isolated modes (see the second panel in the
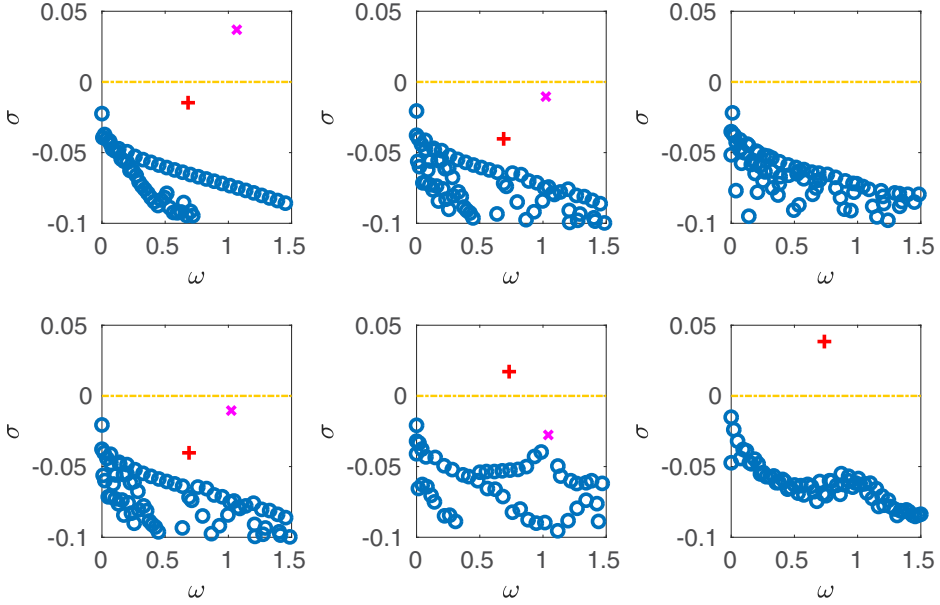
FIG. 3. Eigenspectra for (top) Re = 700 and (from left to right) $h/\delta^* = 2.56, 2.04, 1.70$; (bottom) $h/\delta^* = 2.04$ and (from left to right) Re = 700, 900, 1200. Red crosses indicate sinuous modes, purple stars varicose isolated ones; blue circles represent nonisolated varicose modes.

top row for $h/\delta^* = 2.04$) and then their disappearance from the converged part of the eigenspectrum (top right panel for $h/\delta^* = 1.70$). Further decreasing the shear ratio induces but slight changes to the eigenspectrum (not shown). On the other hand, fixing the shear ratio to $h/\delta^* = 2.04$ and increasing the Reynolds number (bottom row, from left to right) induces the destabilization of a sinuous isolated mode, the critical Reynolds number being Re ≈ 1040, as established in Ref. [9]. Further increasing the Reynolds number up to Re = 1200 causes the disappearance of the isolated varicose mode, whereas the growth rate of the sinuous mode reaches higher values.

The results shown so far indicate that the shear ratio, and more precisely the velocity hitting the cylinder head, plays an important role in the critical Reynolds number at which the steady solution of the three-dimensional Navier-Stokes equations becomes linearly unstable, as well as in the symmetry of the modes prone to instability. The whole picture is summarized in Fig. 4 where the gray (resp. black) region indicates the flow cases in which a sinuous (resp. varicose) mode is globally unstable, whereas the globally stable cases are located in the white zone. Increasing both the Reynolds number and the shear ratio induces a destabilization of the flow, but leading to a different symmetry of the unstable global mode. A similar behavior is obtained with respect to the roughness Reynolds number, as shown in the right panel of Fig. 4: varicose (blue) isolated modes are recovered for large shear ratios, sinuous (red) ones for smaller values, but the latter are destabilized for higher values of the roughness Reynolds number than the former. This clearly indicates that, similarly to the aspect ratio of the roughness element or the roughness Reynolds number, the shear ratio should also be considered as a critical parameter of the system, at least for roughness elements of height comparable with the displacement thickness of the boundary layer, whereas when $h \gg \delta^*$, the shear ratio might not have a distinct influence from the roughness Reynolds number, being $U_{BL}(h) \approx U_\infty$ and thus $\mathrm{Re}_{hh} \approx U_\infty h/\nu = \mathrm{Re}$ no matter the precise value of h. This is also confirmed by the stability diagrams in Fig. 4, where the influence of the shear ratio on the flow stability becomes weaker for the largest values of h/δ^* considered here. In the remainder of the paper we will compare the transition scenarios of two selected cases where the flow is marginally stable with the most unstable modes having different symmetries. In particular, we will focus on
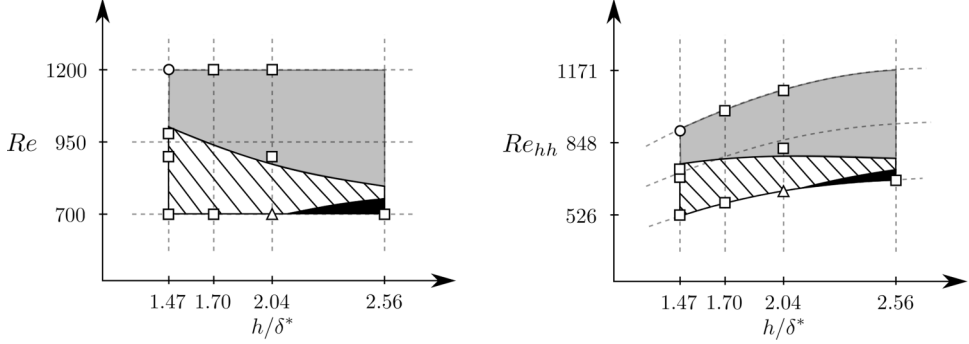
FIG. 4. Stability diagrams: Re (left) and Re_{hh} (right) versus shear ratio. The sketched black regions indicate the flow conditions in which the flow is prone to a varicose unstable mode, the gray one refers to sinuous instability, whereas in the white striped zone the flow is subcritical. The triangles and the circles indicate the cases studied in Refs. [47] and [9], respectively. In all cases the aspect ratio of the roughness elements has been set at $d/h = 1$.

two marginally stable flow cases in which the varicose and sinuous modes have comparable growth rate $\sigma \approx -0.01$, namely, Re = 700, $h/\delta^* = 2.04$ (varicose case, hereafter referred to as VC) and Re = 1000, $h/\delta^* = 1.47$ (sinuous case, hereafter referred to as SC).

IV. RECEPTIVITY TO FREESTREAM TURBULENCE

In this section, we discuss the results of direct numerical simulations forced with increasing levels of freestream turbulence for the two representative operating conditions selected in the previous section. Dynamic mode decomposition and optimal forcing analysis are then carried out to shed some light on the different mechanisms leading the flow to transition to turbulence.

A. Varicose case (Re = 700 and $h/\delta^* = 2.04$)

Let us first consider the varicose case, with Re = 700 and $h/\delta^* = 2.04$. Following prior works, the integral length scale is set to $L = 1.64$ [56], which is related to the wave number k_{max} at which one has the maximum energy $E(k)$ by $L = 1.8/k_{max}$. For the present configuration, the maximum energy is injected at the wave number $k_{max} = 1.09$. Four direct numerical simulations forced by increasingly higher amplitudes of freestream turbulence at the inflow have been conducted. Figure 5 shows the streamwise evolution of the skin friction coefficient $C_f(x)$ for these four cases. In the upstream region of the computational domain (i.e., $x < 0$), the levels of freestream turbulence considered herein have little influence on the skin friction coefficient. In the downstream region of the domain (i.e., $x > 0$), as the intensity of the freestream turbulence increases from 0% to 0.045%, only a slight departure from the laminar state can be observed. Further increasing the intensity to 0.09% amplifies this departure albeit the flow may still be considered as being laminar. Finally, a large departure can be observed for a freestream turbulence intensity of 0.18%, indicating that the flow is experiencing transition to turbulence as shown in Fig. 6. In this figure, one can see the presence of hairpin vortices downstream of the roughness element, which arise despite the linearly globally stable nature of the flow, as also observed experimentally in Ref. [68]. The first train of hairpin vortices is generated in the vicinity of the roughness element as a response to freestream turbulence. These travel and get amplified along the central low-speed streak generated by the blockage effect of the roughness element before eventually fading away at $x \approx 25$. Note additionally that, at $x \approx 15$, inclined vortices begin to be observed on the lateral low-speed streaks, which grow in size while maintaining the spanwise symmetry up to $x \approx 55$. From this point on, breakdown to turbulence occurs and nonsymmetric flow structures are observed. Thus, increasing the turbulence
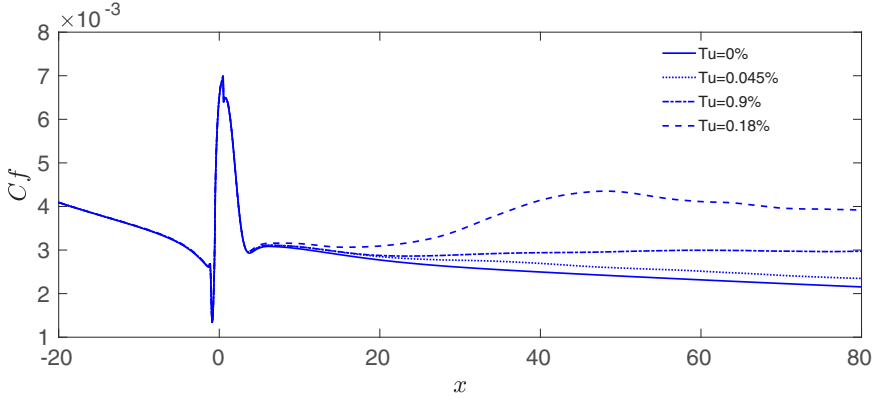
FIG. 5. Streamwise evolution of the skin friction coefficient for different values of Tu in the varicose case $(Re = 700, h/\delta^* = 2.04)$.

intensity considerably affects the flow downstream of the roughness, while modifying the integral length scale for a given value of Tu has been found to provide only negligible effects on the flow dynamics (not shown).

In order to better characterize this transition process, we have performed time Fourier transform of the velocity perturbation at different streamwise locations downstream of the roughness element. For each of the considered streamwise positions, the Fourier spectra provided in the left panel of Fig. 7 show a well-marked high-frequency peak at $\omega \approx 1$, together with its harmonic at $\omega \approx 2$. At streamwise positions sufficiently far from the roughness element, a secondary (weaker) peak emerges at much lower frequency $\omega \approx 0.11$. The shape function of these dominant frequencies of the Fourier spectra are provided in the right panel of Fig. 7, both presenting a varicose symmetry. The Fourier mode with $\omega = 1$ shows alternated high-frequency perturbations starting on the wake region just behind the roughness element, and spreading downstream and toward the lateral streaks. Conversely, the mode with $\omega = 0.11$ presents a low-frequency modulation, mostly localized on the lateral streaks in the downstream part of the domain. These modes will be compared with the DMD modes in the next subsection, where their possible physical origin will be discussed. Moreover, to recover the main wavelengths of the structures created during the transition process, we have performed spatial Fourier transform in the spanwise direction of the velocity perturbation for several streamwise positions. The wall-normal position of the largest Fourier modes as well as their associated spanwise wavelength are reported in Fig. 8. The first peak is linked to the growth of the perturbation on the central low-speed streak, whereas the second one is associated to the growth of the perturbation on the lateral low-speed streaks. The corresponding spanwise wave number is close to $\beta = 0.6$ for both peaks, similar to the value reported in Ref. [47] for an optimally forced DNS. It must be emphasized, however, that as the flow transitions to turbulence, the Fourier spectrum is dominated by modes with $\beta = 0$. Such observation may be indicative that the breakdown of
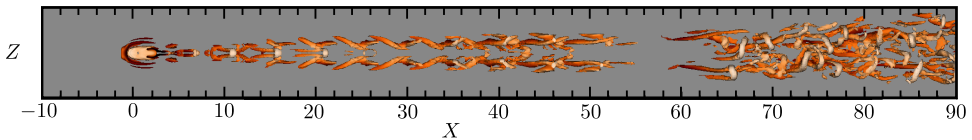

FIG. 6. Snapshot showing the streamwise evolution of the unsteady perturbation in the varicose case with Tu = 0.18%: isolevels of $\lambda_2 = -0.02$ colored by values of the streamwise velocity.
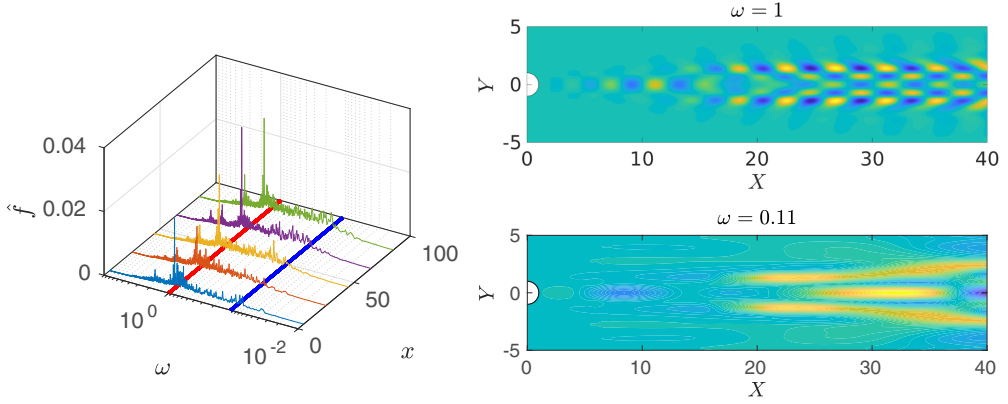
FIG. 7. Left: Time Fourier transform at several streamwise locations for the varicose case. Right: Associated shape function for the dominant frequencies of the Fourier spectrum for (top) $\omega \approx 1$ and (bottom) $\omega \approx 0.11$. The Fourier transform has been performed on velocity signals extracted every $\Delta t = 0.018$ on several cube of probes of size $dx, dy, dz = 0.2$ placed at the streamwise positions reported in the figure. The signals recorded in these probes are averaged in space over dx, dy, dz and rendered periodic before applying the Fourier transform.

the hairpin vortices and the associated mixing eventually give rise to an almost spanwise-invariant distortion of the mean velocity profile.

DMD analysis

The dominant spatiotemporal coherent structures of the flow are extracted by means of dynamic mode decomposition (see Sec. II C). The analyzed data set is made of 500 snapshots of the velocity field sampled every $\Delta T = 0.6$ convective time units. For each snapshot, the strongly turbulent region of the flow given by $x > 50$ is discarded as to facilitate the convergence of the DMD procedure. Hereafter, only the first 21 DMD modes are retained, capturing approximately 92% of
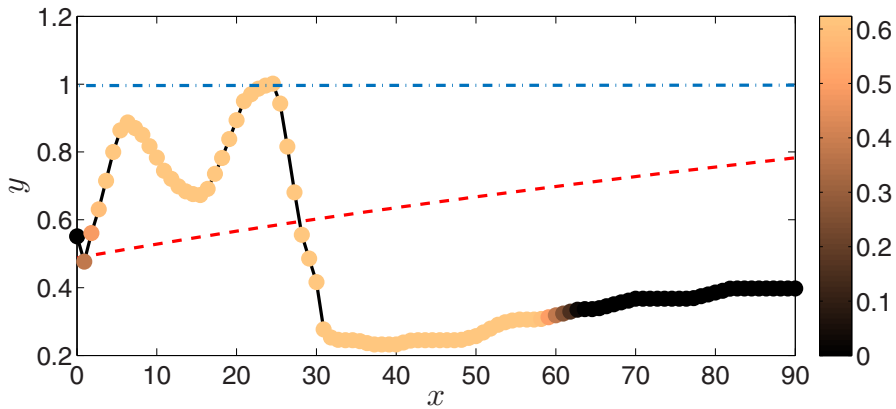

FIG. 8. Streamwise variation of the wall-normal position of the maximum amplitude mode of the spanwise Fourier transform of the root-mean square of the velocity perturbation, u_{rms}. The color bar indicates the values of the spanwise wave number of the dominant Fourier mode. The red dashed line provides the analytical displacement thickness of the Blasius solution whereas the blue dash-dotted line indicates the height of the cylindrical roughness element. Varicose case with Re $= 700$, $h/\delta^* = 2.04$, Tu $= 0.18\%$.
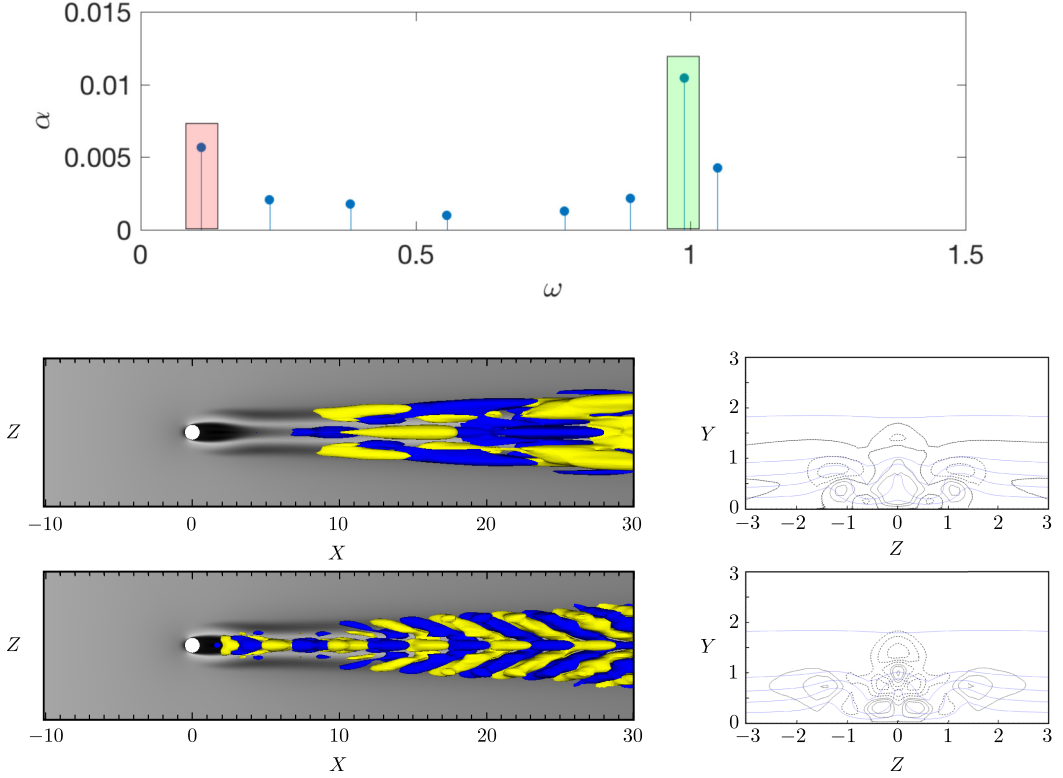
FIG. 9. Top: DMD spectrum providing the dynamic modes with their associated weights. Spatial structure of the modes with (middle row) $\omega \approx 0.11$ and (bottom row) $\omega \approx 1$. On the right column are provided the isolevels of the streamwise velocity perturbation of the DMD modes in the crossflow plane with $x = 10$, whereas the left column shows isosurfaces of the streamwise velocity perturbation ($\pm 5\%$ of the maximum velocity perturbation amplitude).

the perturbation's kinetic energy. Note that the corresponding DMD eigenvalues are characterized by a unit modulus ($|\mu_i| = 1$), or equivalently by a zero temporal growth rate ($\sigma = 0$), conforming the statistical convergence of the flow dynamics. The top panel of Fig. 9 depicts the amplitudes of these dominant DMD modes as a function of the frequency. Two dominant dynamics, associated with $\omega \simeq 1$ and $\omega \simeq 0.11$ are clearly visible, which are fairly close to the dominant frequencies recovered by time Fourier transform. The lower panels of Fig. 9 show the spatial distribution of the corresponding modes, which presents marked similarities with the shape functions associated with the dominant Fourier modes shown in the right panel of Fig. 7. Moreover, the dominant DMD frequency ($\omega \simeq 1$) closely matches that of the least stable varicose eigenmode (see Fig. 3) as well as the most amplified one in the resolvent analysis provided in Ref. [47]. Moreover, the spatial distribution of this DMD mode (see lower panel of Fig. 9) compares favorably with the spatial distribution of the least stable eigenmode of the linearized Navier-Stokes operator provided in Ref. [47]. In the vicinity of the roughness element, the perturbation is essentially localized on top of the central low-speed streak while, moving further downstream, it spreads on the lateral ones in accordance with previously made observations regarding the hairpin vortices and the high-frequency Fourier mode.

Contrary to the aforementioned mode, the one associated with the dominant low frequency $\omega \simeq 0.11$ does not appear to be directly related to the eigenspectrum of the linearized three-dimensional Navier-Stokes operator. Moreover, the pseudospectrum provided in Ref. [47] for the

same flow case considered here shows a well defined peak placed in correspondence with $\omega \approx 1$, while the sensitivity is found to drop by two orders of magnitude at lower (or higher) frequencies. This, together with the Fourier spectra shown in Fig. 7, indicates that the optimal response of the flow in the varicose case is essentially equivalent to a resonator at the frequency $\omega \approx 1$, while a much weaker optimal response is to be expected at lower frequencies. One can notice that the Fourier transform in Fig. 7 shows that the low-frequency mode arises well downstream of the roughness element, indicating its convective nature, whereas the high-frequency one is observed at all streamwise stations, suggesting its connection with a global, resonator-like instability mode. Moreover, although a low-frequency modulation of the leading harmonic dynamics has also been measured experimentally [[47], Fig. 4(a)], no such low-frequency dynamics has been observed in the optimally forced direct numerical simulation [[47], Figs. 16(e) and 16(f)]. This lack of low-frequency unsteadiness in the optimally forced direct numerical simulation suggests that these dynamics may correspond to convective instabilities triggered by the interaction of the boundary layer flow with the external noisy perturbations. Looking at the streamwise velocity disturbance in the $x = 10$ plane, representative of the crossflow distribution of this mode, a double-peaked structure is observed on the low-speed streaks and a near-wall peak in correspondence with the high-speed region, closely recalling the fundamental varicose Tollmien-Schlichting (TS) wave developing on a streaky flow studied in Ref. [69]. A local stability analysis carried out on the $x = 10$ plane, whose details are reported in Appendix C, has recovered three unstable local modes with varicose symmetry at the temporal frequency $\omega = 0.11$. The interaction of these local modes as a consequence of the locally convectively unstable nature of the streaky base flow is likely to generate this low-frequency DMD mode. Moreover, we have verified that the wall-normal profile in the low-speed region has the M-shaped structure observed in Refs. [70,71], further confirming that these modes can be directly associated with the convective instabilities developing on the shear layers of the streaks.

In light of these results, transition induced by freestream turbulence is thus likely to be essentially driven by the global varicose eigenmode even when this mode is globally stable.

B. Sinuous case (Re = 1000 and $h/\delta^* = 1.47$)

Let us now turn our attention to the other flow configuration of interest, now characterized by a leading sinuous eigenmode. The Reynolds number and the shear ratio are fixed to Re = 1000 and $h/\delta^* = 1.47$, respectively. Scaling the previously chosen value of the integral length scale for the current value of h/δ^*, we obtain an integral length scale equal to $L = 3.16$. Computations have been carried out also for $L = 2$ and $L = 4$, showing only slight differences in the transition scenario.

As for the varicose case, four direction numerical simulations forced by increasingly higher amplitudes of freestream turbulence at the inflow of the computational domain have been conducted. Figure 10 shows the streamwise evolution of the skin friction coefficient $C_f(x)$ for these four cases. Once again, the upstream part of the flow (given by $x < 0$) is found to be relatively insensitive to these levels of freestream turbulence. However, the downstream region of the flow now appears to be much more sensitive to freestream turbulence than in the previous case, with a turbulent intensity as low as Tu = 0.06% being able to cause the forced flow to significantly depart from the base flow conditions. Figure 11 illustrates the instantaneous organization of the hairpin-like vortical structures for the highest amplitude of freestream turbulence considered herein. Despite the least stable eigenmode of the linearized Navier-Stokes operator exhibiting a sinuous symmetry for the present operating conditions, the vortical structures behind the roughness element show a clear varicose modulation. As before, these varicose vortical structures get amplified as they travel further downstream before eventually causing the flow to transition to turbulence for $x > 25$.

To characterize the main frequencies of these vortical structures, we have performed time Fourier transform of the velocity perturbation at different streamwise locations downstream of the roughness element. The obtained Fourier spectra, provided in the left panel of Fig. 12, are much broader than in the varicose case, now presenting a main peak at $\omega \approx 0.4$, and a second (slightly weaker) high-
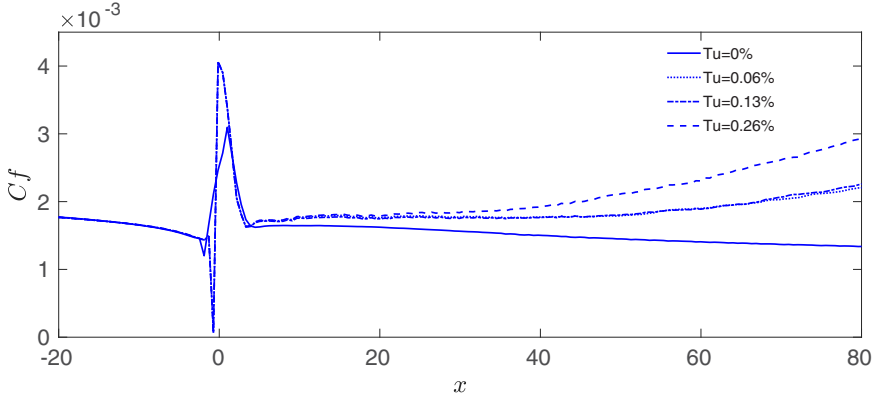
FIG. 10. Streamwise evolution of the skin friction coefficient for different intensities of the freestream turbulence for the sinuous case (Re = 1000, $h/\delta^* = 1.47$). A negligible sensitivity has been found with respect to the integral length scale (not shown).

frequency peak at $\omega \approx 1$–1.2. As before, at streamwise positions sufficiently far from the roughness element, a weaker, low-frequency peak emerges at $\omega \approx 0.15$. Comparing these spectra with those of the varicose case in Fig. 7, one can notice that the peaks are less defined and the dominating frequency and amplitude change in the streamwise direction, suggesting an amplifier-like nature of the flow. The shape functions associated with the lowest and highest dominant frequencies of the Fourier spectra present a similar structure to those recovered in the varicose case (although the latter is localized more downstream) as shown in the right panel of Fig. 12, whereas the Fourier mode with $\omega = 0.4$ shows an intermediate-frequency modulation which originates from the central streak and spreads laterally and downstream. Remarkably, also in the sinuous case all the dominant Fourier modes present a varicose symmetry. The spatial Fourier transform of the velocity perturbation in the spanwise direction has been performed as well. The wall-normal position of the largest Fourier modes as well as their associated spanwise wavelength are reported in Fig. 13. Again, the first peak is linked to the growth of the perturbation on the central low-speed streak, whereas the second one is associated with the growth of the perturbation on the lateral low-speed streaks. However, the second peak is weaker than the first, and is reached farther downstream than in the varicose case. The corresponding spanwise wave number is close to $\beta = 0.6$, similar to the value observed in the previous case as well as to that reported in Ref. [47]. Also in this case once the flow is turbulent, the Fourier spectrum is dominated by spanwise invariant modes with $\beta = 0$.

1. DMD analysis

The top panel of Fig. 14 shows the amplitudes of the DMD modes as a function of the frequency. Quite clearly, this spectrum appears to be more broadband than in the varicose case (see Fig. 9) as also found through time Fourier transform. This spectrum can be broadly categorized in three different frequency ranges ($0.75 < \omega < 0.3$, $0.3 < \omega < 0.8$, and $0.8 < \omega < 1.3$), dominated
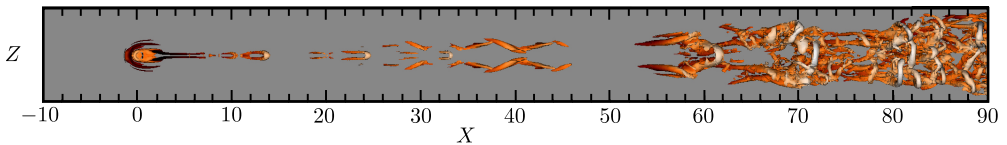

FIG. 11. Snapshot showing the streamwise evolution of the unsteady perturbation in the sinuous case with Tu = 0.26%: isolevels of $\lambda_2 = -0.005$ colored by values of the streamwise velocity.
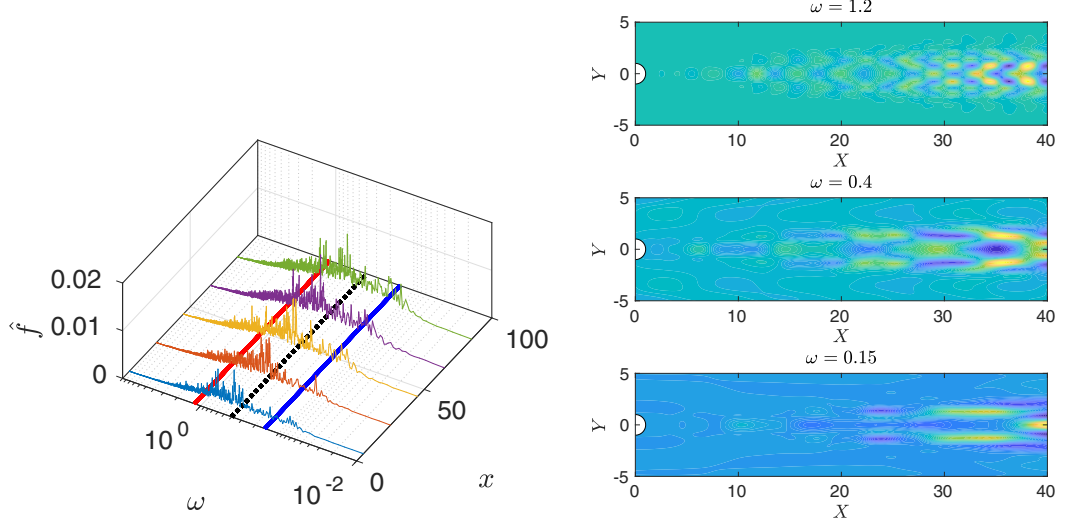
FIG. 12. Left: Time Fourier transform at several streamwise locations for the sinuous case. Right: Associated shape function for (top) $\omega \approx 1.2$, (middle) $\omega \approx 0.4$, and (bottom) $\omega \approx 0.15$. The Fourier transform has been performed on velocity signals extracted every $\Delta t = 0.014$ on several cubes of probes of size $dx, dy, dz = 0.2$ placed at the streamwise positions reported in the figure. The signals recorded in these probes are averaged in space over dx, dy, dz and rendered periodic before applying the Fourier transform.

respectively by the modes associated with $\omega = 0.15, 0.4$, and 1.2, which roughly correspond to the most amplified frequencies recovered in the Fourier spectra. The spatial distribution of these dominating DMD modes is reported in the bottom rows of Fig. 14. It is noteworthy that despite the least stable of the linearized Navier-Stokes operator exhibiting a sinuous symmetry, all of these DMD modes are characterized by a varicose one.
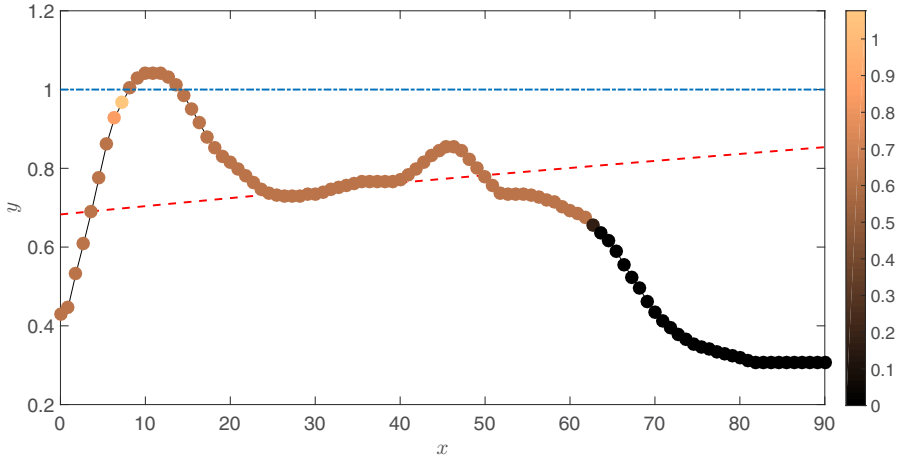

FIG. 13. Streamwise variation of the wall-normal position of the maximum amplitude mode of the spanwise Fourier transform of the root-mean square of the velocity perturbation, u_{rms}. The color bar indicates the values of the spanwise wave number of the dominant Fourier mode. The red dashed line provides the analytical displacement thickness of the Blasius solution whereas the blue dash-dotted line indicates the height of the cylinder. The case considered is the sinuous case with Tu $= 0.26\%$.
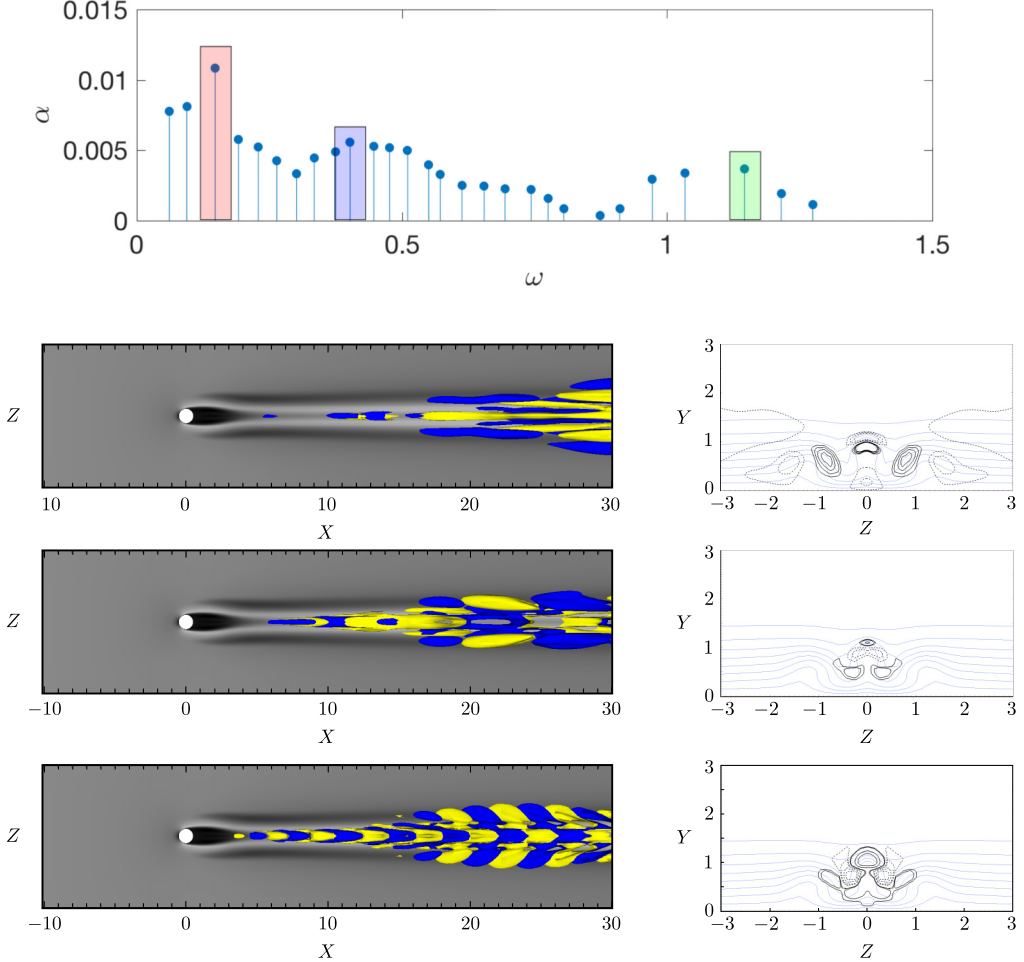
FIG. 14. Top panel: Amplitude of the DMD modes as a function of their frequency. The other panels depict the spatial structure of the modes associated with (second row) $\omega \approx 0.15$, (third row) $\omega \approx 0.4$, and (fourth row) $\omega \approx 1.2$. On the right column are provided the isolevels of the streamwise velocity perturbation of the DMD modes in the crossflow plane with $x = 10$, while the left column shows isosurfaces of the streamwise velocity perturbation ($\pm 5\%$ of the maximum velocity of the perturbation).

The mode associated with $\omega = 0.15$ shares some similarities with the one associated with $\omega = 0.11$ in the varicose case and its origin is thus likely to be ascribed to the development of convective instabilities on top of the streaky boundary layer flow. A local stability analysis carried out on the $x = 10$ plane, reported in Appendix C, has recovered four unstable local modes with varicose symmetry at this particular frequency. Once again, this relatively low-frequency DMD mode is thus likely to be linked to the interaction of these local convective varicose modes. The mode associated with $\omega = 0.4$ (third row) is different from the modes recovered in the varicose case, as well as from all the modes of the spectrum. The physical mechanism at the origin of this mode will be treated later on in Sec. IV B 3. Finally, the DMD mode associated with the highest dominant frequency (bottom row) is similar to the isolated varicose mode found in the previous case, as well as to the optimal forcing computed in Ref. [47]. An optimal forcing analysis carried out for the present flow case and presented below will confirm that this mode is indeed linked to the receptivity of the flow to a varicose mode.
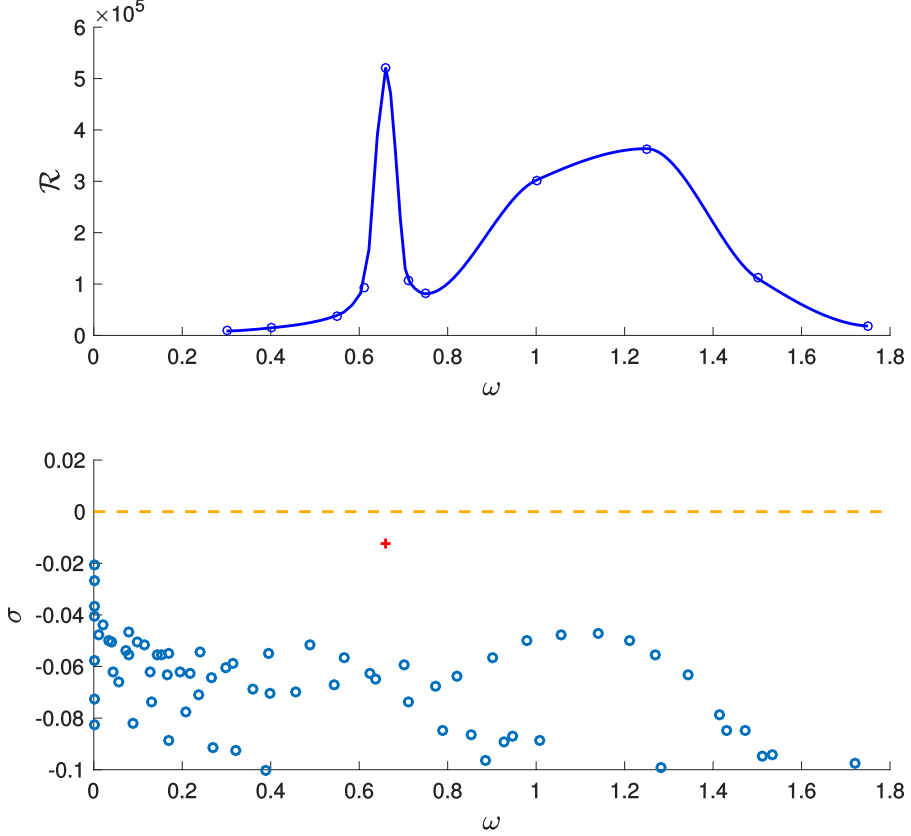
FIG. 15. Top: Resolvent norm versus forcing frequency. Bottom: Eigenspectrum for the sinuous case. $(+)$ sinuous mode associated with $\omega = 0.68$, $(\circ)$ varicose modes.

2. Optimal forcing analyses

In order to shed light on the origin of the dynamic mode associated with the circular frequency $\omega = 1.2$, a resolvent analysis is conducted. Figure 15 depicts the eigenspectrum of the linearized Navier-Stokes operator for these particular operating conditions (bottom panel) as well as the evolution of the resolvent gain $\mathcal{R}(\omega)$ as a function of the forcing frequency (top panel). The resolvent norm highlights that the flow is highly receptive at the frequency $\omega = 0.65$ corresponding to the eigenfrequency of the isolated sinuous eigenmode. Figure 16 provides a side by side comparison of the direct and adjoint sinuous eigenmodes obtained from the eigenvalue decomposition of the linearized Navier-Stokes operator (top panel) and of the optimal forcing and associated response obtained from the resolvent analysis (bottom panel). As can be seen, these two pairs of modes are very similar, thus strongly suggesting that the high gain exhibited by the resolvent at the frequency $\omega = 0.65$ is likely to result solely from the resonance of this particular eigenmode, as has been observed in Ref. [47] for the varicose case considered in Sec. IV A. Nonetheless, it is worthy to note that despite the high receptivity of the sinuous instability to a harmonic forcing at its eigenfrequency, no such coherent structure has been recovered from the DMD analysis of the nonlinear dynamics. This apparent contradiction may however easily be explained by the fact that the free-stream turbulence imposed in the direct numerical simulation actually injects very little energy at this particular frequency. Consequently, although this sinuous mode may exist in the data, its amplitude is so low that it plays little to no role in the transition process and cannot be easily captured by the DMD analysis.
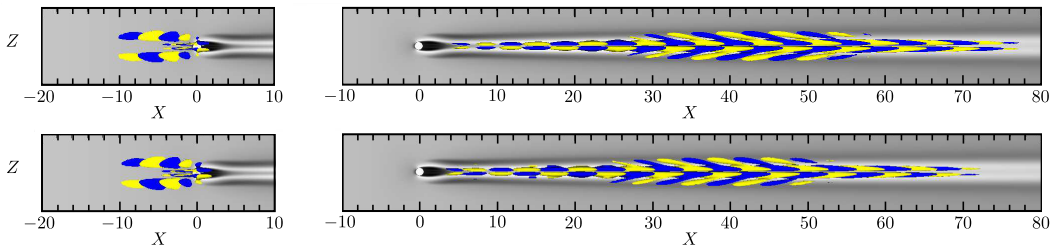
FIG. 16. Top: Sinuous mode at $\omega = 0.68$ (right) and its adjoint counterpart (left). Bottom: Optimal forcing (left) and response (right) for the same value of ω in the sinuous case. The isosurfaces show the $\pm 5\%$ of the maximum amplitude of the streamwise velocity perturbation.

The second feature of interest exhibited by the resolvent norm is the large amplification of the frequency range $0.8 \leqslant \omega \leqslant 1.6$. Comparing it with the eigenspectrum shown in the bottom panel of Fig. 15, it is remarkable that this range of frequencies overlaps precisely with the range over which a branch of varicose eigenmodes exists. Additionally, it also corresponds to the third frequency range observed from the DMD analysis (see Fig. 14). In all of these cases, the peak in the high-frequency range is found at $\omega \simeq 1.2$.

Figure 17 provides a side by side comparison of the direct and adjoint eigenmodes from the varicose branch exhibiting the largest growth rate (top panel) and of the optimal forcing and associated response obtained from the resolvent analysis (bottom panel). Although these two pairs of modes show some similarities, they do not compare as favorably as the sinuous ones do. Rather than being related to the resonance of a single eigenmode, the broadband amplification observed for $0.8 \leqslant \omega \leqslant 1.6$ thus is directly resulting from the high non-normality of the linearized Navier-Stokes operator. Given the good agreement between this second feature of the resolvent norm and the third frequency range extracted from DMD analysis, these results strongly suggest that for the present operating conditions, the transition to turbulence is essentially governed by the high receptivity of varicose coherent structures to broadband turbulence.

3. Optimal perturbation

The last feature of the DMD analysis to remain unexplained is the mild peak observed around $\omega \simeq 0.4$. Looking at Fig. 15, it is clear that the resolvent does not exhibit a large amplification at this particular frequency and the behavior of the system at $\omega \simeq 0.4$ cannot hence be explained by high receptivity to harmonic forcing. We thus turn our attention toward optimal perturbation analysis (i.e., finding the initial condition inducing the largest transient energy growth over a given time) conjecturing that the $\omega \simeq 0.4$ dynamics might result from transient growth of wave
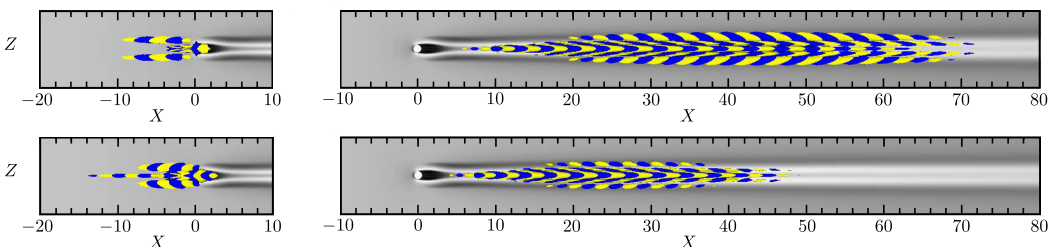

FIG. 17. Top: Varicose mode for $\omega = 1.25$ (right) and its adjoint counterpart (left). Bottom: Optimal forcing (left) and response (right) for $\omega = 1.2$ for the sinuous case. The isosurfaces show the $\pm 5\%$ of the maximum amplitude of the streamwise velocity perturbation.
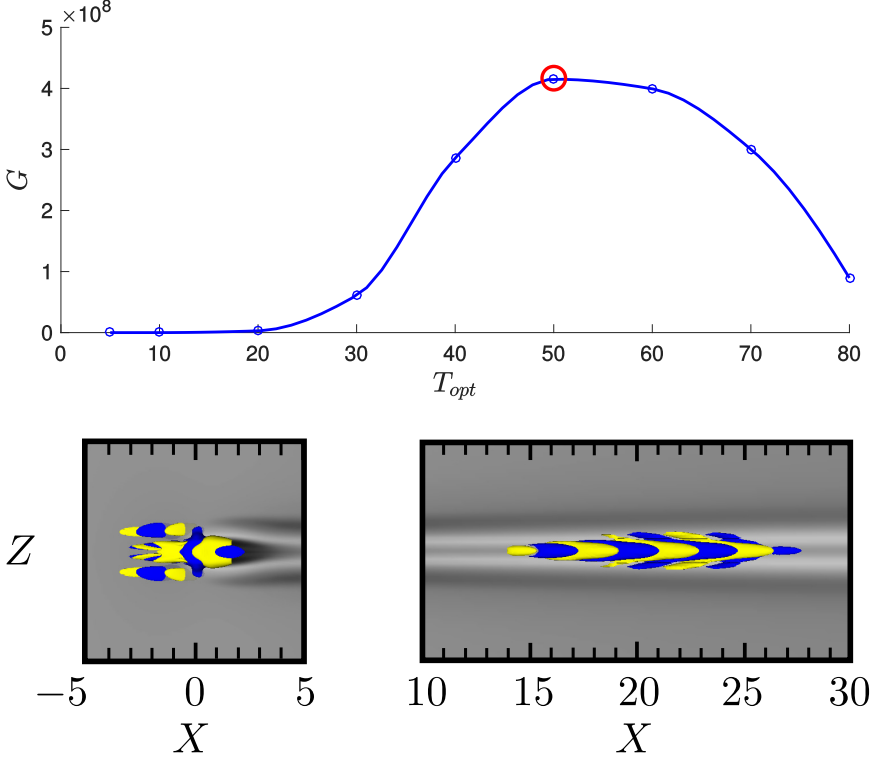
FIG. 18. Top: Optimal energy gain curve, with maximum gain equal to 4.3×10^8 at $T_{\text{opt}} = 50$. Bottom: Optimal perturbation at $t = 0$ (left) and $t = T_{\text{opt}} = 50$ (right). The isosurfaces represent the $\pm 5\%$ of the maximum amplitude of the streamwise velocity perturbation. Sinuous case with $Re = 1000$, $h/\delta^* = 1.47$.

packets produced by freestream turbulence upstream of the roughness element. As discussed in Refs. [72,73], when the optimal perturbation has a much larger gain than the suboptimal one, it is likely that the environmental noise would project in time onto this strongly amplified perturbation, populating the flow of structures resembling the optimal one. Toward this aim, we thus compute the initial perturbation $\boldsymbol{u}_0 = \boldsymbol{u}(\boldsymbol{x}, 0)$ maximizing at a given target time T_{opt} the energy gain

$$G(T_{\text{opt}}) = \max_{\boldsymbol{u}_0} \frac{E(T_{\text{opt}})}{E(0)} \tag{9}$$

with the kinetic energy $E(t)$ being

$$E(t) = \frac{1}{2} \int_V \boldsymbol{u}(\boldsymbol{x}, t) \cdot \boldsymbol{u}(\boldsymbol{x}, t) dV. \tag{10}$$

The initial perturbation is supposed to have infinitesimal amplitude; thus its dynamics is governed by the linearized Navier-Stokes equations in Eq. (3). The initial optimal perturbation and the consequent optimal response at time T_{opt} have been evaluated computing the first eigenvalue and eigenvector of $\mathbf{M}^\dagger(T_{\text{opt}})\mathbf{M}(T_{\text{opt}})$ and $\mathbf{M}(T_{\text{opt}})\mathbf{M}^\dagger(T_{\text{opt}})$, respectively, following the procedure in Sec. II D. The dependency of the linear optimal energy gain with respect to the target time is shown in the top panel of Fig. 18. A maximum gain G_{max} of order 10^8 is reached at $T_{\text{opt}} = 50$. The corresponding initial and final optimal perturbations are shown in the lower panel of Fig. 18. One can notice the resemblance (at least in the near-wake region) of the final perturbation with the DMD mode associated with the frequency $\omega = 0.4$ shown in Fig. 14 (third row). Both are characterized by alternated positive/negative patches of streamwise perturbation placed on top of the low-velocity
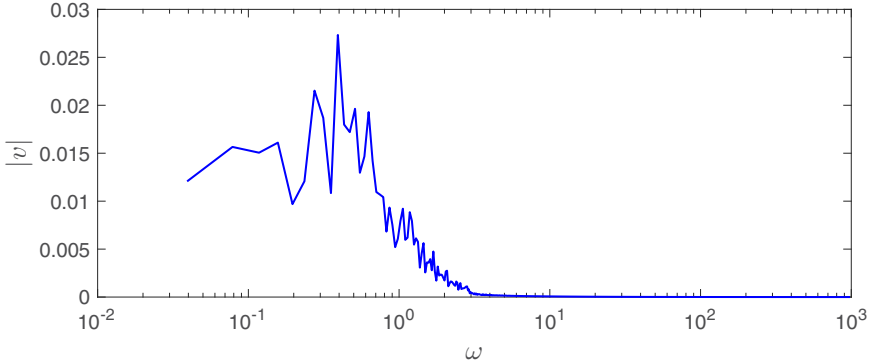
FIG. 19. Fourier transform in time of the wall-normal velocity measured at a probe placed at $(x, y, z) = (10, 1, 0)$ in a DNS initialized with the optimal perturbation for $T_{opt} = 50$. Sinuous case with Re $= 1000$, $h/\delta^* = 1.47$.

central speed streak. As might be expected, being issued from a linear transient growth analysis at a rather low target time, the optimal perturbation remains confined in the near wake, whereas the corresponding DMD mode extracted from a nonlinear simulation spreads downstream to the lateral streaks (see also the discussion at the end of Sec. V). Initializing a DNS using the corresponding initial optimal perturbation, letting it evolve freely in time, and Fourier-transforming the wall-normal velocity signal extracted at $(x, y, z) = (10, 1, 0)$, we obtain the Fourier spectrum in Fig. 19. A peak value is recovered for $\omega = 0.4$, suggesting that the DMD mode having the same frequency might be indeed linked to the development of quasioptimal perturbations from wave packets initially created from the freestream turbulence upstream of the cylinder. Even if these wave packets would not match the initial optimal perturbation computed here, they will project in time onto the optimal perturbation as explained in Ref. [72], giving rise to the DMD mode with $\omega \simeq 0.4$.

V. TRANSITION

In the previous section, we have established that unsteadiness at subcritical Reynolds number results from the high receptivity of the varicose global modes, even when a sinuous global mode is close to being marginally unstable. The subsequent nonlinear evolution of these perturbations into trains of hairpin vortices however needs further analysis. In the following, we will analyze how the base flow is distorted toward the mean flow once the unsteadiness is triggered as a consequence of the excitation of the varicose global modes due to freestream turbulence. This analysis will be carried out for the flow case at (Re, h/δ^*) $= (700, 2.04)$, but similar conclusions can be drawn for the other flow cases analyzed here, except for the sinuously unstable cases such as that already analyzed in Ref. [9].

A. Linear mechanism

As a first step, we determine the regions of the flow where transition is initiated by inspecting the energy production regions of the most unstable varicose mode. Toward this aim we use the Reynolds-Orr equation

$$\frac{dE}{dt} = -\int_V u_i u_j \frac{\partial U_i}{\partial x_j} dV - \frac{1}{\text{Re}} \int_V \frac{\partial u_i}{\partial x_j} \frac{\partial u_i}{\partial x_j} dV, \qquad (11)$$

where the Cartesian tensor notation with the Einstein convention has been used for brevity, u_i and U_i being the perturbation and base flow velocity components, respectively, and x_i being the spatial coordinates x, y, z. The two terms on the right-hand side of Eq. (11) represent the production of

perturbation energy due to extraction from the base flow and the energy dissipation due to viscous effects, respectively. The production term can be decomposed in nine contributions of the Reynolds stress tensor, which are all nonzero due to the three-dimensionality of the base flow. Following Ref. [74], these nine terms can be reduced down to four by decomposing the perturbation into

$$\boldsymbol{u}(\boldsymbol{x}, t) = \boldsymbol{u}_\perp(\boldsymbol{x}, t) + \boldsymbol{u}_\parallel(\boldsymbol{x}, t),$$

where $\boldsymbol{u}_\perp$ is the component of the perturbation perpendicular to the base flow field and $\boldsymbol{u}_\parallel$ is the parallel one. These two components are defined as

$$\boldsymbol{u}_\parallel = \frac{(\boldsymbol{u} \cdot \boldsymbol{U}_b)}{\|\boldsymbol{U}_b\|^2} \boldsymbol{U}_b; \quad \boldsymbol{u}_\perp = \boldsymbol{u} - \boldsymbol{u}_\parallel. \tag{12}$$

Injecting this decomposition into the Reynolds-Orr equation (11) leads to the following four production terms:

$$I_{1V} = \int_V I_1 dV = \int_V \boldsymbol{u}_\perp \cdot (\boldsymbol{u}_\perp \cdot \boldsymbol{\nabla}) \boldsymbol{U}_b \, dV,$$

$$I_{2V} = \int_V I_2 dV = \int_V \boldsymbol{u}_\parallel \cdot (\boldsymbol{u}_\perp \cdot \boldsymbol{\nabla}) \boldsymbol{U}_b \, dV,$$

$$I_{3V} = \int_V I_3 dV = \int_V \boldsymbol{u}_\perp \cdot (\boldsymbol{u}_\parallel \cdot \boldsymbol{\nabla}) \boldsymbol{U}_b \, dV,$$

$$I_{4V} = \int_V I_4 dV = \int_V \boldsymbol{u}_\parallel \cdot (\boldsymbol{u}_\parallel \cdot \boldsymbol{\nabla}) \boldsymbol{U}_b \, dV. \tag{13}$$

Because the base flow downstream of the cylindrical roughness element is streaky, $\boldsymbol{u}_\parallel$ is aligned with the streaks in that region while $\boldsymbol{u}_\perp$ is in-plane with the counter-rotating vortices. The contribution of each of these four productions terms (normalized by dissipation) to the total kinetic energy budget is displayed in the top left panel of Fig. 20. Most of the energy production is provided by the term I_2, corresponding to the lift-up production term [13]. This production term characterizes the exchange of energy from the counter-rotating vortices to the streaks. Comparatively, the anti-lift-up production term (I_3) and the counter-rotating vortex (I_1) and streak (I_4) self-production terms have much smaller value. The right panel of Fig. 20 shows the streamwise evolution of the dominating production term (I_2) integrated along the crossflow planes downstream of the roughness element. The production of the varicose mode peaks at $x \approx 10$ before decreasing toward zero at $x \approx 40$. As also shown in the bottom panels of Fig. 20, the region wherein the largest production occurs is placed in the shear region at $y \approx 1$ along the central low-speed streaks behind the roughness element. In this region, the streamwise vorticity perturbation transports the central streak low momentum toward the lateral high-speed streaks, destabilizing the flow for sufficiently high values of the Reynolds number. For the operating conditions considered herein, although the Reynolds number is not sufficiently high to trigger global instability, the varicose mode is excited by receptivity to external disturbances. Interestingly, in the near-wake region the streamwise distribution of energy production follows closely the root-mean-square fluctuating velocity value $u_{\rm rms}$ measured experimentally in Ref. [44] by a probe at $(y, z) = (1, 0)$. Hence, in this near-wake region, velocity fluctuations are indeed produced by the varicose stable modes. How these fluctuations evolve into hairpin vortices will be discussed in the next subsection.

B. Hairpin vortices

Let us consider the base flow topology sketched in Fig. 21. The flow passing by the roughness element generates a horseshoe vortex pair (HP) wrapping around the roughness. At the same time, a secondary flow is induced when the flow turns around the cylinder. A particle ideally placed in the position **A** of the sketch will move to position **B** under the effect of the centrifugal forces. Due to the presence of the HP vortex a particle in **B** will then move toward **C** thanks to the momentum
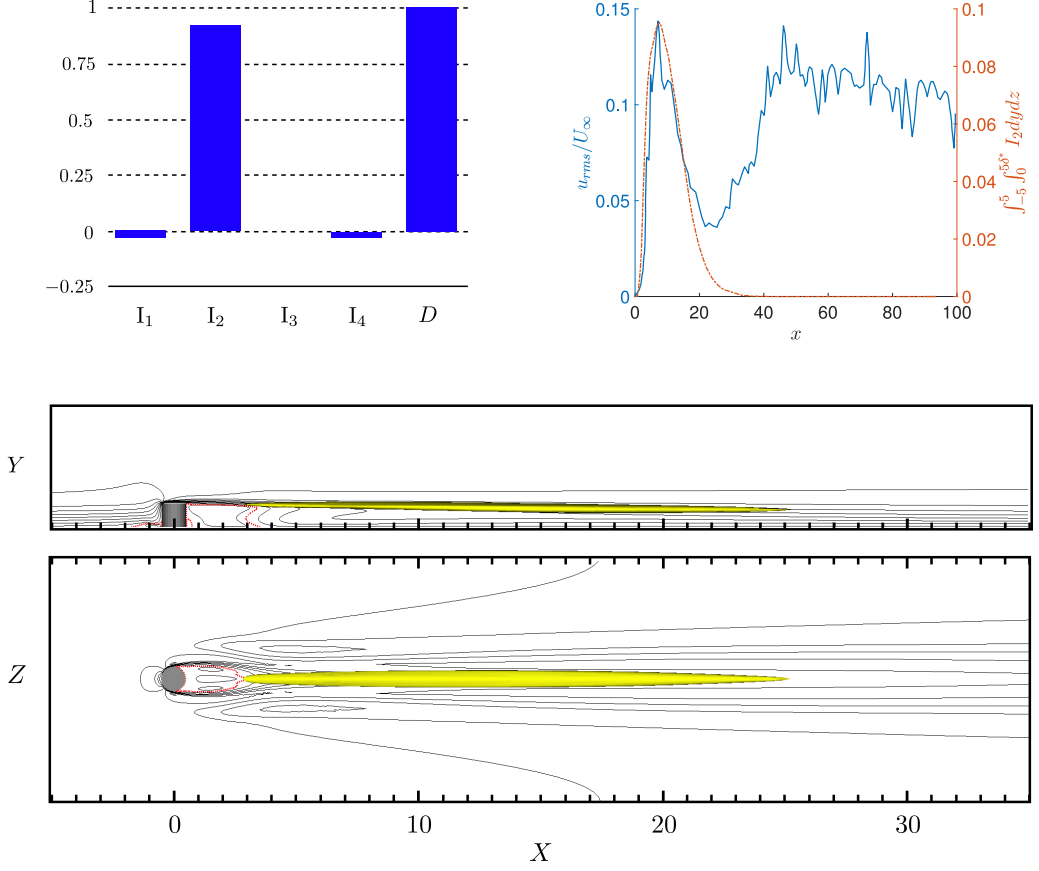
FIG. 20. Top left: Kinetic energy budget normalized with respect to the dissipation. Top right: Comparison of the perturbation root-mean-square value u_{rms} measured experimentally by a probe at $(y, z) = (1, 0)$ with the evolution of the crossflow integral of the I_2 production term in the streamwise direction. Bottom: Spatial distribution of the lift-up production term. Varicose case $\mathrm{Re} = 700$ and $h/\delta^* = 2.04$ forced by freestream turbulence of intensity $\mathrm{Tu} = 0.18\%$.

diffusion. Just behind the roughness element, a positive pressure gradient in the spanwise direction, $\partial p/\partial z$, is generated by the presence of the separation zone. The particle is then pushed from **C** to **D**. Finally, the particle in **D** will now have a low inertia; thus, for mass conservation, it will move from **D** to **A**. Due to the combination of these effects, a new pair of vortices, dubbed the *rear pair* (RP) vortices, is generated. The *rear pair* vortices have also been observed experimentally in the flow past roughness elements of different shapes [75]. In the considered configuration, HP and RP vortices can be easily visualized by passive Lagrangian tracking of particles injected in the inflow and transported by the base flow field as shown in Fig. 22. Particles are injected at $x = -15$, $z = 0.1$, and distributed along y from 0.1 to 0.7. A subset of particles is captured by the core of the horseshoe vortex, while the residual ones enter in the recirculation zone remaining locked in the core of the rear pair vortex. The RP vortices have little influence on the far field since they are dissipated when the low-speed streak in the symmetry plane disappears (i.e., at $x \approx 20$), as one can observe looking at the streamwise vorticity (Ω_x) in the $y = 0.5$ plane in Fig. 23 (top panel). Nevertheless, the RP vortices are a necessary ingredient for the hairpin vortex generation close to the roughness element. To understand the mechanisms involved in the hairpin creation we refer to Ref. [76], whose authors proposed a minimal model for the generation of packets of
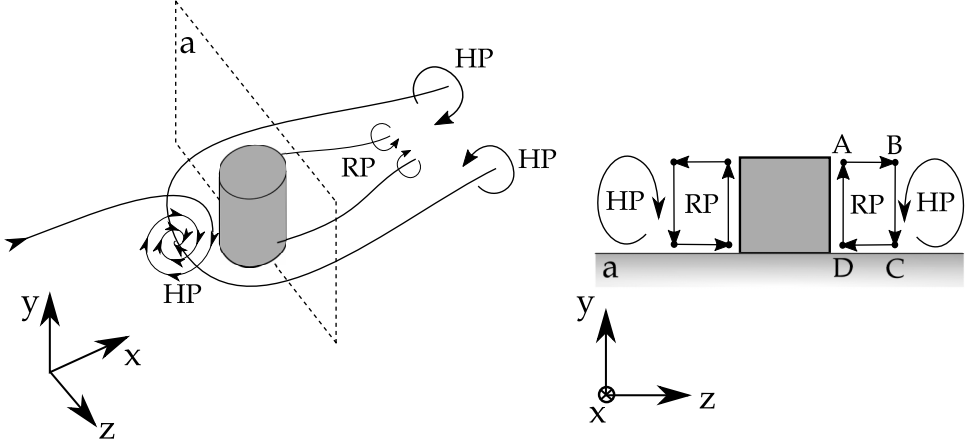
FIG. 21. Sketch explaining the physical mechanism for the generation of the rear pair vortices (RP). Points labeled B, C, D represent the successive positions of a particle initially placed in A and HP indicates the horseshoe vortex wrapping the roughness.

hairpin vortices. They conjectured that hairpin vortices are generated by the nonlinear interaction of three structural ingredients, namely a shear in the wall-normal direction, a counter-rotating vortex pair (CVP), and a two-dimensional wavy vortex sheet [[76], Fig. 2]. Looking at the velocity field just behind the cylindrical roughness element in Fig. 23, the first element of the model, i.e., the counter-rotating vortex pair represented by the RP vortices, can easily be identified. Moreover, in
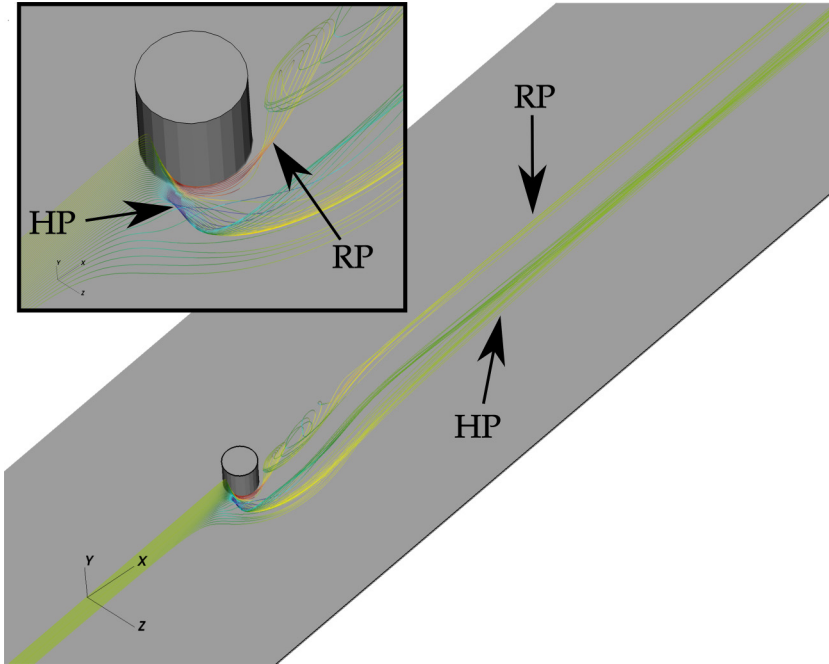

FIG. 22. Passive particle tracking in the base-flow field: Some of the particles are trapped by the rear pair vortices (RP); the remaining particles are advected by the horseshoe vortices (HP). Varicose case with Re = 700 and $h/\delta^* = 2.04$.
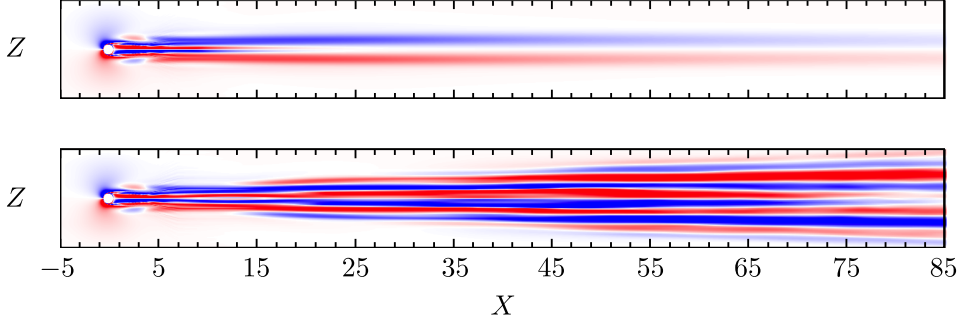
FIG. 23. Streamwise vorticity $\Omega_x \pm 0.5$ in the plane $y = 0.5$ of the (top) base flow and (bottom) mean flow computed from the DNS in the presence of freestream turbulence with Tu = 0.18%. Varicose case at Re = 700 and $h/\delta^* = 2.04$.

Fig. 24, we can observe that the mean flow is characterized by a strong wall-normal shear already at $x = 5$ due to the reverse flow in the recirculation bubble. In particular, evaluating the regions where $\partial^2 U / \partial y^2 + \partial^2 U / \partial z^2 = 0$ allows us to locate inflection points in the streamwise velocity profiles indicated by black circles in Fig. 24. One of the inflection points is placed at $y = 1$, i.e., in the wall-normal region where the production of the global mode is large (see Fig. 20). At this wall-normal position, a peak of the spanwise vorticity indicating the presence of hairpin heads can be observed. The generation of hairpin heads in correspondence with the inflection points suggests, as conjectured in Ref. [77] for a channel flow experiencing K-type transition, that hairpin vortices are generated as a consequence of varicose inflectional instability of the mean velocity profile distorted by a negative perturbation in the streamwise velocity. Similar observations have been made in Ref. [78] for optimally growing hairpin-shaped perturbations. The wall-normal shear decreases moving downstream and one of the inflection points of the mean flow disappears at $x = 10$. This position is the one at which the production of the varicose mode, as well as the u_{rms} values, begins to decrease. Thus, in the near-wake region ($0 < x < 10$), once the global varicose mode is triggered by receptivity, it gives rise to a wavy vortex sheet which interacts with the rear pair vortices as well as the inflection points of the separated region, constituting the three ingredients of the model proposed in Ref. [76] enabling the generation of nonlinear hairpin vortices.
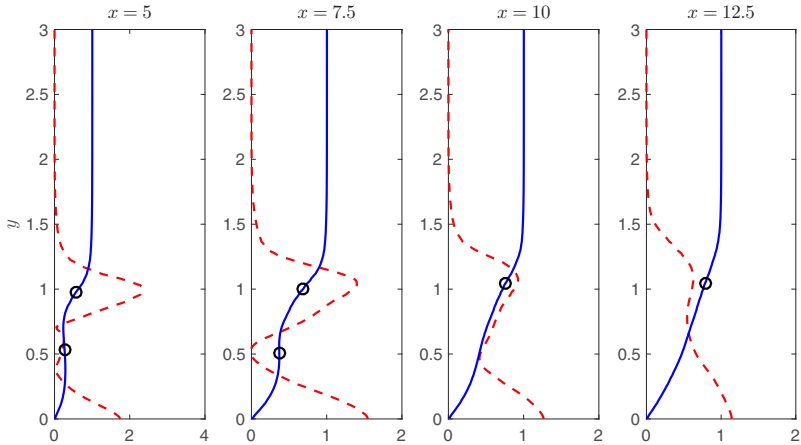

FIG. 24. Streamwise evolution of the streamwise velocity (blue line) and of the module of spanwise vorticity (red line) of the mean flow in the plane $z = 0$. The circles indicate the inflectional points according to the Rayleigh Fjørtoft criterion.
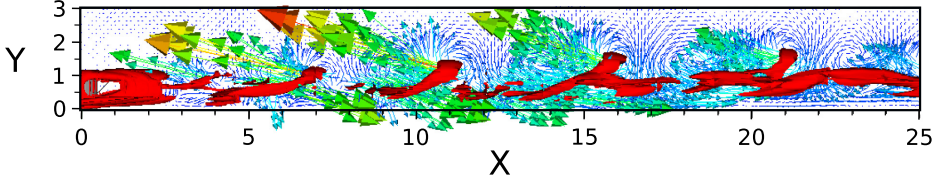
FIG. 25. Snapshot of transition extracted from the DNS showing the vortical structures (isosurfaces of $\lambda_2 = -0.02$) and the velocity field (arrows) in the symmetry plane.

C. Late stages of transition

Once generated, hairpin vortices are advected and stretched in the streamwise direction as shown by the isocontours of the λ_2 criterion in Fig. 25. Figure 25 also provides the velocity vectors in the $z = 0$ midplane, highlighting the presence of sweep and ejection events under the head of the hairpin vortices [79]. For $x > 20$, as one can observe in Fig. 6, hairpin vortices on the low-speed streak begin to fade away, sweep events close to the wall being no longer sustained by the presence of inflection points in the base flow velocity profile. At the same time, new vortical structures appear between the high-speed streak and the low-speed streaks. In order to investigate the origin of such lateral vortices, the streamwise evolution of the amplitude of the low- and high-speed streaks is measured. Following [80], the integral streak amplitude can be measured as

$$A_{ST}(x) = \frac{1}{U_\infty} \int_{-1/2}^{+1/2} \int_0^{\eta^*} |U(x, y, z) - U^z(x, y)| d\eta \, d\zeta, \tag{14}$$

where

$$\eta = \frac{y}{\delta} = \frac{y}{\sqrt{x\nu/U_\infty}}, \quad \eta^* = 9, \text{ and } \zeta = \frac{z}{L_z}, \tag{15}$$

$U^z(x, y)$ being the streamwise velocity averaged in the crossflow direction. The measured values of A_{ST} are reported in Fig. 26 for the considered flow case. While the central low-speed streak rapidly fades away, reaching zero amplitude at $x \approx 20$, the lateral low- and high-speed streaks slowly increase in strength in the streamwise direction, reaching approximately the same amplitude
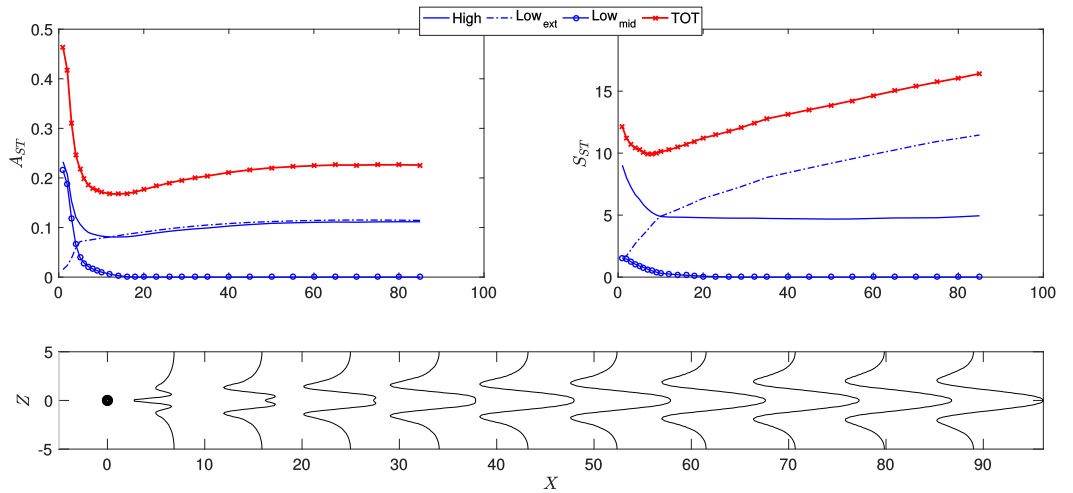

FIG. 26. Streamwise variation of the (left) amplitude of the streaks and of the (right) area associated with the streaks for the base flow.

for $x > 20$. However, A_{ST} being an integral quantity, its value must be weighted by the crossflow area occupied by the considered streaks. Indeed, streaks having the same integral amplitude but occupying a larger (smaller) crossflow area are associated with weaker (stronger) velocity values. The crossflow area associated with the high-speed (low-speed) streaks is computed by evaluating the crossflow regions having positive (negative) values of the integrand of Eq. (14). Variation in the streamwise direction of the crossflow area occupied by the low- and high-speed streaks is shown in the right panel of Fig. 26. While the crossflow area of the lateral low-speed streaks remains approximately constant in the streamwise direction, that occupied by the high-speed streaks increases considerably as we move downstream. High-speed streaks thus increase their strength while moving downstream, whereas low-speed ones keep approximately constant velocity values but spread laterally. This lateral spreading can be seen by paying attention to the deviation of the base flow with respect to the Blasius solution provided in the bottom panel of Fig. 26. Due to the increasing high-speed velocity deviation, an inflection of the streamwise velocity is created in the shear region between the central high-speed and the lateral low-speed streaks. This inflection point does not fade away in the streamwise direction, but slowly moves laterally in the spanwise direction, as one can see in the bottom panel of Fig. 26. In this region, lateral vortical structures that wrap around the two lateral low-speed streaks are generated (see Fig. 6 for $x > 20$) and move outward in the z direction. This explains the lateral spreading of the vortical perturbation while moving downstream, with the generation of multiple vortices in the spanwise direction, as one can see in Fig. 23 providing the streamwise vorticity field for the mean flow.

VI. SUMMARY AND DISCUSSION

In this work, we have studied the effect of freestream turbulence on the transition process of a boundary-layer flow hitting a cylindrical roughness element mounted at the wall. One of the main aims has been to investigate how the Reynolds number and the ratio of the roughness's height to boundary layer thickness (namely, the shear ratio) affects the transition process. To do so, we have used the joint application of direct numerical simulations, dynamic mode decomposition, and linear modal and nonmodal stability tools. Previous works [9] have indicated that thin cylinders (i.e., with aspect ratio $\eta = d/h \leqslant 1$, d being the diameter and h the height of the roughness element) are prone to a global instability exhibiting a sinuous symmetry, whereas varicose global instability is found for thicker cylinders having $\eta > 1$. The present analysis has highlighted that there exist particular conditions in which also for thin cylinders (with $\eta = 1$), the leading eigenmode is characterized by a varicose symmetry. This happens when the height of the roughness element is sufficiently larger than the boundary layer's displacement thickness δ^*, namely, for $h/\delta^* > 2.04$. These results complete those reported in Ref. [9], where it was shown that, for fixed shear ratio h/δ^*, the symmetry of the leading eigenmode depends essentially on the aspect ratio of the roughness element. Here, we fixed the aspect ratio of the cylinder and scanned the two-dimensional parameter space spanned by the Reynolds number Re and the shear ratio h/δ^*, showing that the latter has a prominent role in the onset and symmetry of the primary instability and of the consequent transition scenario that the flow will experience. It must be noted additionally that other studies [10] focusing on miniaturized hemispherical roughness elements have also reported that the ratio h/δ^* appears to play a key role in the selection of the varicose or sinuous symmetry of the dominant instability as well as on the critical Reynolds number at which the flow becomes linearly unstable. Finally, while the onset of the sinuous instability in terms of the roughness Reynolds number Re_h appears to be less sensitive to the shear ratio, the interplay between the critical roughness Reynolds number and shear ratio h/δ^* needs further analysis.

However, as established by several studies [9,10,81,82], global stability analysis is only able to provide an estimation for the upper bound of the transition diagram based on several literature results reported in Ref. [33], whereas a clear understanding of the physical mechanisms governing subcritical transition, allowing a prediction of the lower bound of the transition diagram, is still lacking. Recently, in Ref. [47] it has been shown that for certain operating conditions, subcritical

transition may be explained by a resonance of a marginally stable eigenmode forced by external excitations. In this work, we have moved one step forward compared to Ref. [47] by simulating the response of the flow in the presence of freestream turbulence and trying to explain the resulting observations by the joint applications of optimal perturbation and resolvent analysis. For that purpose, two representative operating conditions, each characterized by a marginally stable eigenmode exhibiting a different symmetry, have been considered. In both cases, the forcing induced by freestream turbulence gives rise to varicose coherent structures in the wake of the roughness element eventually causing transition to turbulence further downstream. The varicose case having been studied extensively in Ref. [47], the current work focuses most of its attention on the case characterized by a marginally stable sinuous eigenmode. Despite the existence of this marginally stable eigenmode, no sinuous coherent structures are observed in the forced direct numerical simulation, nor detected by dynamic mode decomposition, which has shown instead that the flow is governed by three types of varicose dynamics. At low frequencies ($\omega \simeq 0.1$), a varicose coherent structure reminiscent of Tollmien-Schlichting waves in streaky boundary layer flows is observed. In the highest frequency range ($0.8 \leqslant \omega \leqslant 1.6$), resolvent analysis has highlighted that the corresponding varicose structures observed in the direct numerical simulation are resulting from the high sensitivity to harmonic forcing of a branch of varicose eigenmodes whose amplification is directly related to the non-normality of the Navier-Stokes operator. Unsteadiness has been also observed in intermediate frequency range ($\omega \simeq 0.4$) albeit resolvent analysis has been unable to elucidate its physical origin. Optimal perturbation analysis has however revealed that these intermediate frequency dynamics could result from localized wave packets excited by the freestream turbulence, which transiently grow as they travel downstream. Despite the linearly stable nature of the base flows, our simulations have shown shedding of hairpin vortices downstream of the roughness elements. The consequent transition scenario has been investigated, showing that the origin of unsteadiness is to be found in the near-wake region, where the energy production of the varicose eigenmodes is localized. In this region, due to the high receptivity of the flow, the spanwise-symmetric global modes are excited by the freestream turbulence. This provides a wavy vortex sheet that interacts with the rear-pair vortices and with the wall-normal shear of the base flow, originating hairpin vortices that are shed downstream, consistent with the minimal model for their generation proposed in Ref. [76]. The hairpin vortices grow downstream on the low-velocity middle streak, sustained by the presence of inflectional points in the wall-normal direction. When the central low-speed streak disappears, the hairpin vortices are dissipated but vortical perturbation are spread on the two lateral low-speed streaks due to the presence of a spanwise shear. The growth of the lateral streaks intensifies the spanwise shear allowing the spreading of vortices in the spanwise direction as well, strongly deforming the base flow into a highly vortical mean flow.

This investigation indicates that linear sensitivity analyses are able to educe the physical mechanisms responsible for the onset of unsteadiness at subcritical Reynolds number, at least for the low freestream turbulence intensities used in the present work. These results strongly underline that the lower bound for transition reported in the diagram of Ref. [33] may indeed result from the rise of globally stable, highly sensitive varicose modes which are excited by the inherent low-amplitude free turbulence existing in most of the experimental setups.

Existing results from the literature and those presented in this work put in the limelight that, depending on the operating conditions, the roughness-induced boundary layer flow may behave either as a noise amplifier (present work), a resonator [47], or a flow oscillator [9,10,81,82]. These results moreover underline that the roughness Reynolds number and the aspect ratio of the roughness element may not be the only important parameters to characterize the flow. Although practical, the transition diagram proposed in Ref. [33] (considering only these two parameters) may thus be too simplistic to enable good predictions. In light of these recent results, we would thus advocate that a better understanding could be obtained by investigating the properties of the flow in the four-dimensional parameter space spanned by the roughness Reynolds number Re_h, the aspect ratio of the protuberance η, the shear ratio h/δ^*, and the freestream turbulence intensity Tu. Finally, the shape of the protuberance may also play a crucial role in the transition process, albeit this is mostly
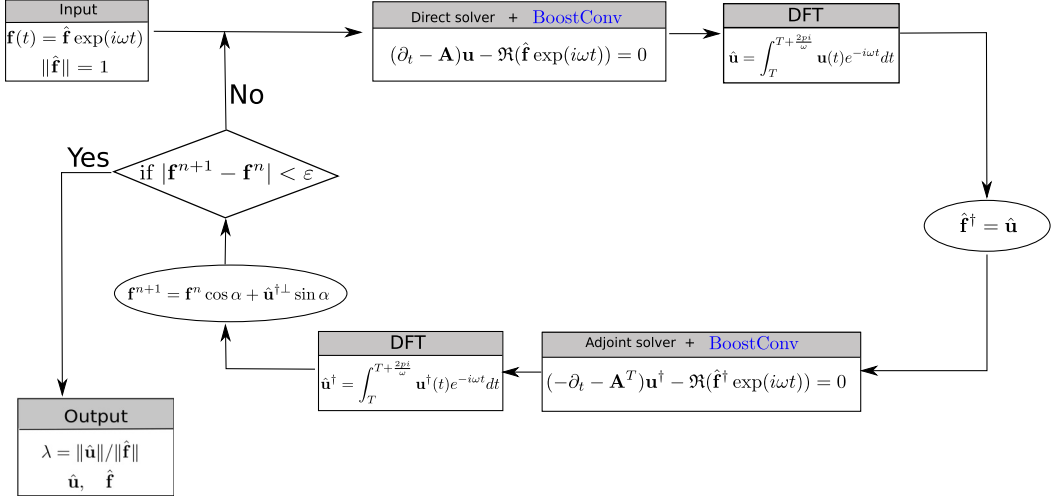
FIG. 27. Sketch of the optimization loop used for obtaining the optimal forcing/response.

unexplored at the moment as parametrizing the shape would increase the dimensionality of the parameter space to be investigated exponentially fast. This is thus left for future work.

APPENDIX A: OPTIMAL FORCING ALGORITHM AND VALIDATION

The response $\hat{\boldsymbol{u}}$ of the system with respect to the forcing $\boldsymbol{f} = \hat{\boldsymbol{f}} e^{i\omega t}$ + c.c. (in the absence of unstable global modes) is given by Eq. (7). In a three-dimensional problem as that considered here, the inverse of the matrix $i\omega\boldsymbol{I} - \boldsymbol{A}$ cannot be computed directly due to the huge memory requirements, or by using a Hessenberg matrix constructed by a time-marching procedure since the equation to be solved is not time-dependent. Thus, the resolvent norm is optimized using the method proposed by [67], which formulates the problem as an optimization of the following Lagrange functional,

$$\mathcal{L}(\hat{\boldsymbol{u}}, \hat{\boldsymbol{u}}^\dagger, \lambda, \hat{\boldsymbol{f}}) = \underbrace{\langle \hat{\boldsymbol{u}}, \hat{\boldsymbol{u}} \rangle}_{\text{objective}} \underbrace{- \langle \hat{\boldsymbol{u}}^\dagger, (i\omega\boldsymbol{I} - A)\hat{\boldsymbol{u}} - \hat{\boldsymbol{f}} \rangle - \lambda(\langle \hat{\boldsymbol{f}}, \hat{\boldsymbol{f}} \rangle - 1)}_{\text{constraints}}, \tag{A1}$$

having as objective function the kinetic energy of the response, and the forced linearized Navier-Stokes equations as well as the the amplitude of the forcing (normalized to 1) set as constraints. Note that no time integral is present and that the adjoint variable $\hat{\boldsymbol{u}}^\dagger$ is assumed to be harmonic. The variation of the augmented functional with respect to the Lagrange multipliers (or adjoint variables) $\hat{\boldsymbol{u}}, \hat{\boldsymbol{u}}^\dagger, \lambda$, and $\hat{\boldsymbol{f}}$ gives

$$\frac{\partial \mathcal{L}}{\partial \hat{\boldsymbol{u}}} := (-i\omega\boldsymbol{I} - A^\dagger)\hat{\boldsymbol{u}}^\dagger - \hat{\boldsymbol{u}} = 0, \tag{A2a}$$

$$\frac{\partial \mathcal{L}}{\partial \hat{\boldsymbol{f}}} := \hat{\boldsymbol{f}} - \lambda^{-1}\hat{\boldsymbol{u}}^\dagger = 0, \tag{A2b}$$
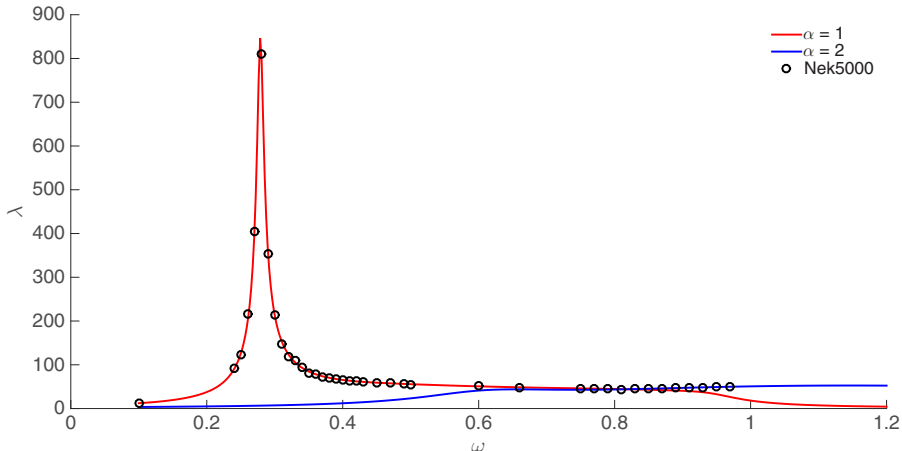
FIG. 28. Resolvent norm obtained using the present numerical code (circles) compared to that obtained by a local resolvent analysis for two values of the streamwise wave number ($\alpha = 1$, red line, and $\alpha = 2$, blue line) for the Poiseuille flow at Re $= 4000$. The resolvent gain obtained with the present analysis is the envelope of the resolvent gain curves obtained with the local theory for different values of the streamwise wave number.

which represent the adjoint resolvent as well as the optimality condition used to update the forcing during the iterative optimization loop; see [67] for further details. Initializing a numerical simulation with a zero perturbation velocity field and a random unitary forcing and running the simulation for a sufficiently long time, it is possible to recover the complex response $\hat{\boldsymbol{u}}$ by performing a Fourier transform of the perturbation velocity field over one forcing period. The optimization loop proposed by [67] and modified in order to accelerate the convergence is depicted in Fig. 27. To minimize the number of iterations required to reach convergence, a gradient-rotation method [83,84] has been used. For properly converging the optimal forcing analysis at the value of $\omega = 0.3$ we employed 5 214 522 Navier-Stokes iterations ($\times 2$ for the adjoint evaluation) divided into 12 direct-adjoint loops, corresponding to 589 824 CPU hours on 2048-core processors. For a ω value half that mentioned here, at least a double integration time will be needed, leading to an exponential increase of the computational hours needed for converging the computation reaching ≈ 1.2M CPU hours, which are far beyond our computational capabilities. Convergence is achieved when the gradient norm falls below 10^{-5} or the difference of the resolvent gain between two successive iterations is less than 10^{-8}. Moreover, to reduce the time needed by the direct numerical simulation to reach a time periodic behavior before performing the Fourier transform, we have used the BoostConv algorithm proposed by [66], which can be used to find periodic base flows as shown by [85]. The main idea is to select a proper Poincaré plane in which the periodic behavior is forced to be stationary, by properly building the Krylov space as

$$\boldsymbol{X}_k = [\boldsymbol{u}(t_0), \boldsymbol{u}(t_0 + T_p), \ldots, \boldsymbol{u}(t_0 + (k-1)T_p)]. \tag{A3}$$

We have validated the optimal forcing procedure using as a test case the 2D Poiseuille flow. In particular, we have compared the results obtained by the present optimal forcing code with those obtained using local stability theory for different streamwise wave numbers α. The main results are shown in Fig. 28 for Re $= 4000$. Since the iterative method presented here is able to recover only

TABLE II. Setup of case 1 in Ref. [2].

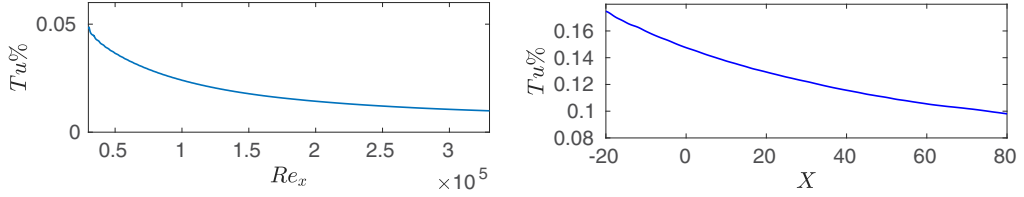| $x \times y \times z$	$nx \times ny \times nz$	$Re_{\delta*}$	Tu (%)	L/δ^*
$1000 \times 100 \times 90$	$1152 \times 201 \times 192$	300	4.7	5

FIG. 29. Exponential Tu decay for case 1 in Ref. [2] (left panel) and for the case $(\mathrm{Re}, h/\delta^*) = (700, 2.04)$ considered in this work. The curve is extracted at $y/\delta^* = 60$.

the optimal solution (i.e., no suboptimal), the resolvent gain curve obtained with the previously discussed numerical procedure follows the gain curve obtained with the local resolvent analysis for streamwise wave number $\alpha = 1$ when $\omega < 0.8$, switching to that obtained with $\alpha = 2$ when $\omega > 0.8$. The shape of the optimal response and forcing also compares very well (not shown).

APPENDIX B: FREESTREAM TURBULENCE VALIDATION

As to validate the procedure to generate synthetic freestream turbulence, we have reproduced the DNS of boundary-layer transition to turbulence induced by inlet freestream turbulence by [2]. In particular, we have used the set of parameters corresponding to case 1 in Ref. [2], which are reported in Table II. A total of 133 980 spectral elements with a spectral order equal to 12 are used in NEK5000 to achieve the same solution depicted in Ref. [2]. The exponential Tu decay with the streamwise direction is shown in Fig. 29, which compares well with Fig. 2 in Ref. [2]. The turbulent intensity $\mathrm{Tu} = \sqrt{(u_{\mathrm{rms}}^2 + v_{\mathrm{rms}}^2 + w_{\mathrm{rms}}^2)/3}$ is evaluated at $y/\delta^* = 60$ and averaged in the z direction. The turbulence decay obeys a power law as observed experimentally. A further validation is provided by computing the skin friction coefficient C_f versus Re_x as shown in Fig. 30, which compares well with Fig. 3(a) in Ref. [2]. Note that the theoretical Blasius (laminar) C_f and the empirical turbulent one are also reported in the figure since the C_f value is used to indicate the transition position. Finally, the instantaneous flow field is shown in Fig. 31, providing the streamwise velocity field extracted on the wall-normal plane at $y/\delta^* = 2$. The streak generation induced by the lift-up mechanism and the streak instability with the generation of turbulent spots can be noticed in Fig. 31. Finally, the right frame of Fig. 29 shows the exponential turbulence decay found for the case $(\mathrm{Re}, h/\delta^*) = (700, 2.04)$ considered in this work.
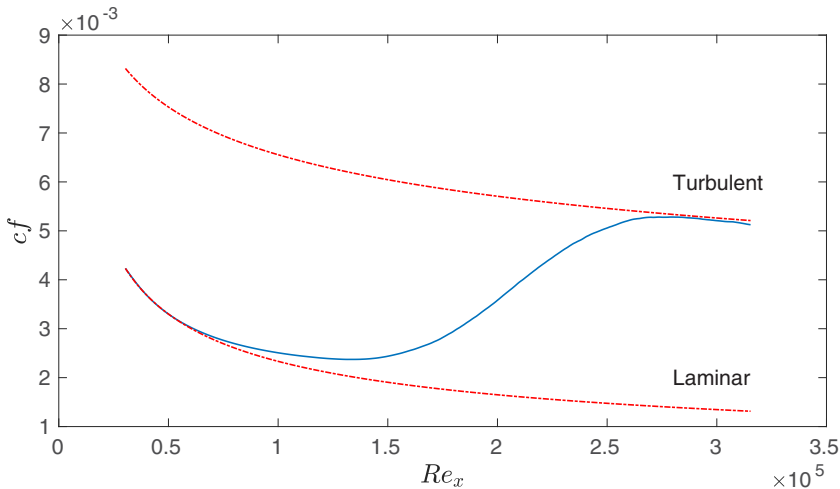

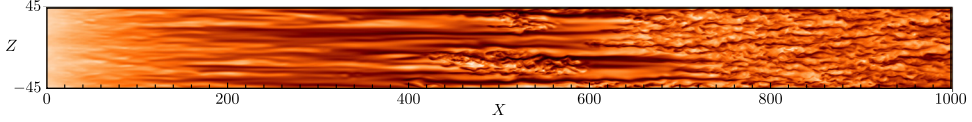FIG. 30. Skin friction coefficient C_f versus Re_x for case 1 in Ref. [2].

FIG. 31. Instantaneous streamwise velocity field at $y/\delta^* = 2$ for case 1 in Ref. [2].

APPENDIX C: BILOCAL STABILITY ANALYSIS

In this Appendix we report the results of a bilocal stability analysis carried out on the $x = 10$ plane for both cases under consideration. In the VC, bilocal stability analysis has recovered three unstable local modes with varicose symmetry, and two with sinuous symmetry, whose frequencies and growth rates are provided in Table III. We can notice that a low-frequency mode exists, called V_1, having temporal frequency close to that of the low-frequency DMD mode with $\omega = 0.11$. However, the spatial distribution of this DMD mode, shown in the middle panel of Fig. 9, compares more favorably with the higher-frequency local varicose modes shown in the bottom right panel of Fig. 32. Both modes are essentially localized on top of the central low-speed streak and on the high-shear regions of the lateral ones, whereas the intermediate varicose modes, V_2, despite being characterized by rather higher frequencies, present a structure similar to V_1, although the former is more extended on the lateral streaks. The similarities in frequency or spatial structure, between the low-frequency DMD mode and the varicose local modes, suggest that these dynamics may be linked to the interplay of different convective instabilities triggered by the interaction of the boundary layer flow with the external noisy perturbations.

In the SC, bilocal stability analysis has recovered four unstable local modes with varicose symmetry, and three with sinuous symmetry, whose frequencies and growth rates are provided in Table III. The lowest-frequency mode here has a rather higher pulsation than in the VC, approximately doubling that of the low-frequency DMD mode with $\omega \approx 0.15$. The spatial distribution of this DMD mode, shown in the middle panel of Fig. 9, compares favorably with the lowest-frequency local varicose modes shown in the top right panel of Fig. 33. Once again, both modes are essentially localized on top of the central low-speed streak and on the high-shear regions of the lateral ones. The other varicose modes, not shown here for brevity, present a similar overall structure, although they are more or less extended in the spanwise direction and some of them present an opposite spatial distribution of the positive/negative perturbation patches.

TABLE III. Pulsation, growth rate, and streamwise wave number for the 5 unstable modes found by bilocal stability analysis at $x = 10$ in the varicose case.
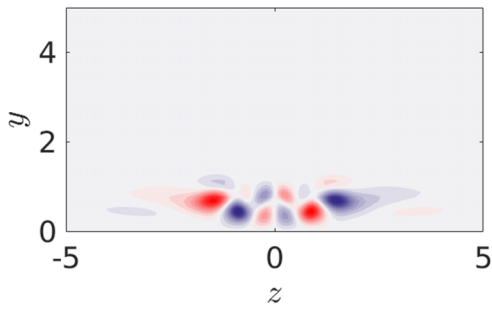
Modes	Varicose Case				Sinuous Case		
	ω_i	ω_r	α		ω_i	ω_r	α
V_1	0.19	0.009	0.45		0.34	0.065	0.8
V_2					0.57	1.11	3.6
S_2					0.65	0.19	3.4
V_3	0.48	0.03	0.90		0.63	0.063	1.2
S_3	0.48	0.04	0.85		0.75	0.05	1.5
V_4	0.65	0.06	1.05		1.35	0.48	5.1
S_4	0.84	0.064	1.20		1.69	0.26	5.6
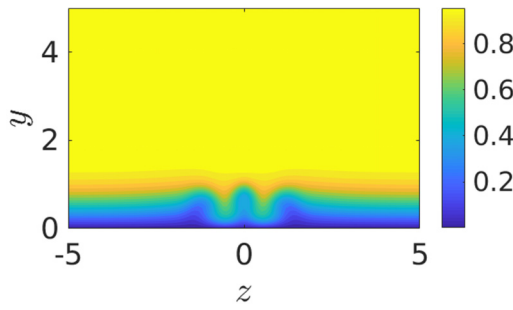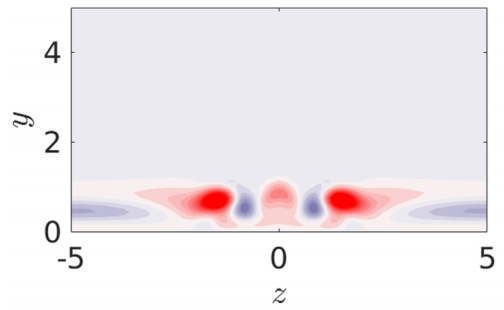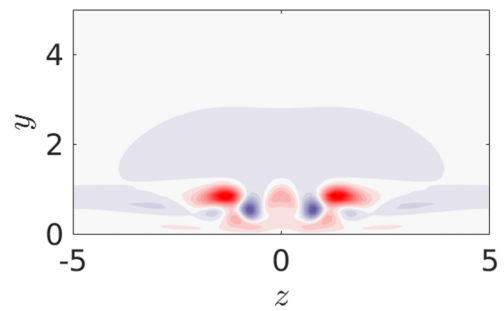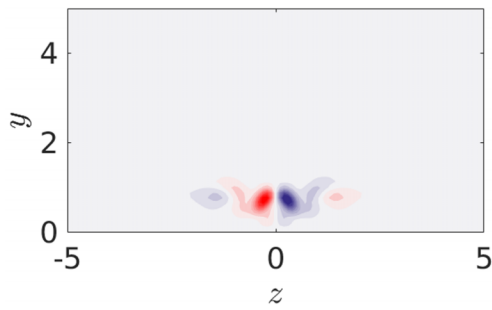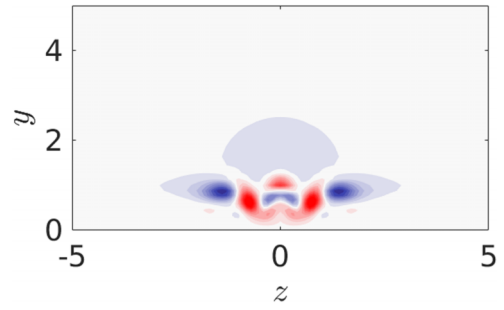
FIG. 32. Base flow of the varicose case at $x = 10$ used for the bilocal stability analysis (top left) and corresponding varicose (right column) and sinuous (left column) unstable modes.
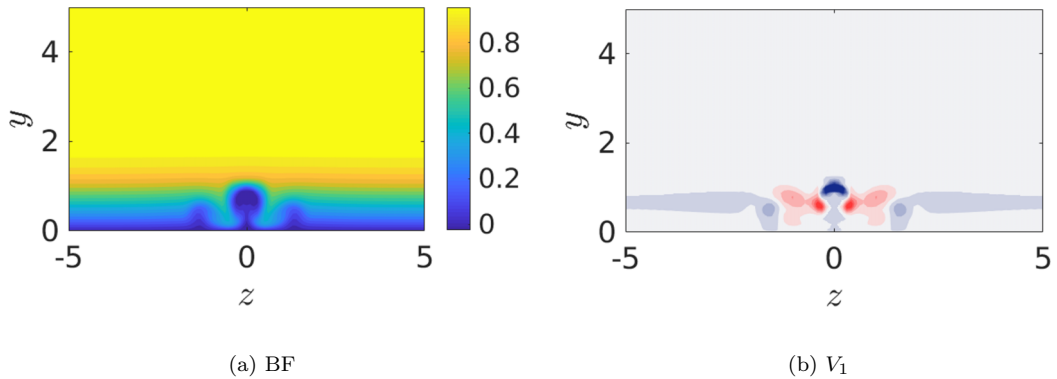
(a) BF   (b) V_1

FIG. 33. Base flow of the sinuous case at $x = 10$ used for the bilocal stability analysis (left) and corresponding varicose low-frequency unstable mode, V_1 (right).

[1] M. V. Morkovin, On receptivity to environmental disturbances, in *Instability and Transition*, edited by M. Hussaini and R. G. Voigt (Springer, Berlin, 1990), pp. 281–295.

[2] L. Brandt, P. Schlatter, and D. S. Henningson, Transition in boundary layers subject to free-stream turbulence, J. Fluid Mech. **517**, 167 (2004).

[3] T. Lee, M. Fisher, and W. H. Schwarz, Investigation of the effects of a compliant surface on boundary-layer stability, J. Fluid Mech. **288**, 37 (1995).

[4] H. Wedin, S. Cherubini, and A. Bottaro, Effect of plate permeability on nonlinear stability of the asymptotic suction boundary layer, Phys. Rev. E **92**, 013022 (2015).

[5] S. Ghosh, J.-C. Loiseau, W.-P. Breugem, and L. Brandt, Modal and non-modal linear stability of poiseuille flow through a channel with a porous substrate, Eur. J. Mech. B: Fluids **75**, 29 (2019).

[6] F. Picella, J. Robinet, and S. Cherubini, Laminar-turbulent transition in channel flow with superhydrophobic surfaces modelled as a partial slip wall, J. Fluid Mech. **881**, 462 (2019).

[7] P. Klebanoff and K. Tidstrom, Mechanism by which a two-dimensional roughness element induces boundary-layer transition, Phys. Fluids **15**, 1173 (1972).

[8] J. H. M. Fransson, L. Brandt, A. Talamelli, and C. Cossu, Experimental and theoretical investigation of the nonmodal growth of steady streaks in a flat plate boundary layer, Phys. Fluids **16**, 3627 (2004).

[9] J.-C. Loiseau, J.-C. Robinet, S. Cherubini, and E. Leriche, Investigation of the roughness-induced transition: Global stability analyses and direct numerical simulations, J. Fluid Mech. **760**, 175 (2014).

[10] V. Citro, F. Giannetti, P. Luchini, and F. Auteri, Global stability and sensitivity analysis of boundary-layer flows past a hemispherical roughness element, Phys. Fluids **27**, 084110 (2015).

[11] N. T. Gregory and W. S. Walker, *The Effect on Transition of Isolated Surface Excrescences in the Boundary Layer* (HM Stationery Office, Aeronautical Research Council Reports & Memoranda, Cranfield, UK, 1956).

[12] C. J. Baker, The laminar horseshoe vortex, J. Fluid Mech. **95**, 347 (1978).

[13] M. Landahl, A note on an algebraic instability of inviscid parallel shear flows, J. Fluid Mech. **98**, 243 (1980).

[14] R. D. Joslin and C. E. Grosch, Growth characteristics downstream of a shallow bump: Computation and experiments, Phys. Fluids **7**, 3042 (1995).

[15] P. Fischer and M. Choudhari, Numerical simulation of roughness induced transient growth in a laminar boundary layer, in *34th AIAA Fluid Dynamics Conference* (AIAA, AIAA Reston, USA, 2004).

[16] A. Tumin and E. Reshotko, Receptivity of a boundary-layer flow to a three-dimensional hump at finite Reynolds numbers, Phys. Fluids **17**, 094101 (2005).

[17] F. G. Ergin and E. B. White, Unsteady and transitional flows behind roughness elements, AIAA J. **44**, 2504 (2006).

[18] N. A. Denissen and E. B. White, Roughness-induced bypass transition revisited, AIAA J. **46**, 1874 (2008).

[19] A. M. Naguib, J. F. Morrison, and T. A. Zaki, On the relationship between the wall-shear-stress and transient-growth disturbances in a laminar boundary layer, Phys. Fluids **22**, 054103 (2010).

[20] N. Denissen and E. White, Secondary instability of roughness-induced transient growth, Phys. Fluids **25**, 114108 (2013).

[21] M. A. Kegerise, R. A. King, M. Choudhari, F. Li, and A. T. Norris, An experimental study of roughness-induced instabilities in a supersonic boundary layer, in *7th AIAA Theoretical Fluid Mechanics Conference* (AIAA, AIAA Reston, USA, 2014).

[22] M. Choudhari, F. Li, C.-L. Chang, J. Edwards, M. Kegerise, and R. King, Laminar-turbulent transition behind discrete roughness elements in a high-speed boundary layer, in *48th AIAA Aerospace Sciences Meeting* (AIAA, AIAA Reston, USA, 2010).

[23] M. M. Choudhari, F. Li, M. D. Bynum, M. A. Kegerise, and R. A. King, Computations of disturbance amplification behind isolated roughness elements and comparison with measurements, in *45th AIAA Fluid Dynamics Conference* (AIAA, AIAA Reston, USA, 2015).

[24] A. Chou, M. A. Kegerise, and R. A. King, Transition induced by streamwise arrays of roughness elements on a flat plate in Mach 3.5 flow, J. Fluid Mech. **888**, A21 (2020).

[25] A. Di Giovanni and C. Stemmer, Cross-flow-type breakdown induced by distributed roughness in the boundary layer of a hypersonic capsule configuration, J. Fluid Mech. **856**, 470 (2018).

[26] Y. Liu, T. A. Zaki, and P. A. Durbin, Floquet analysis of secondary instability of boundary layers distorted by Klebanoff streaks and Tollmien-Schlichting waves, Phys. Fluids **20**, 124102 (2008).

[27] M. J. P. Hack and T. A. Zaki, Streak instabilities in boundary layers beneath free-stream turbulence, J. Fluid Mech. **741**, 280 (2014).

[28] P. Ricco, J. Luo, and X. Wu, Evolution and instability of unsteady nonlinear streaks generated by free-stream vortical disturbances, J. Fluid Mech. **677**, 1 (2011).

[29] P. Ricco, E. J. Walsh, F. Brighenti, and D. M. McEligot, Growth of boundary-layer streaks due to free-stream turbulence, Int. J. Heat Fluid Flow **61**, 272 (2016).

[30] S. Shahinfar, S. S. Sattarzadeh, J. H. M. Fransson, and A. Talamelli, Revival of Classical Vortex Generators Now for Transition Delay, Phys. Rev. Lett. **109**, 074501 (2012).

[31] L. Siconolfi, V. Citro, F. Giannetti, S. Camarri, and P. Luchini, Towards a quantitative comparison between global and local stability analysis, J. Fluid Mech. **819**, 147 (2017).

[32] L. Klanfer and P. R. Owen, The effect of isolated roughness on boundary layer transition, Royal Aircraft Establishment, RAE Tech. Memo 355, 1953.

[33] A. E. von Doenhoff and A. L. Baslow, *Boundary Layer and Flow Control, Its Principles and Application: The Effect of Distributed Surface Roughness on Laminar Flows* (Pergamon Press, Oxford, UK, 1961), pp. 657–681.

[34] I. Tani, H. Komoda, and Y. Komatsu, Boundary-layer transition by isolated roughness, Technical Report No. 375, Aeronautical Research Institute, University of Tokyo, 1962.

[35] P. S. Klebanoff, W. G. Cleveland, and K. D. Tidstrom, On the evolution of a turbulent boundary layer induced by a three-dimensional roughness element, J. Fluid Mech. **237**, 101 (1992).

[36] E. Piot, G. Casalis, and U. Rist, Stability of the laminar boundary layer flow encountering a row of roughness elements: Biglobal stability approach and DNS, Eur. J. Mech. B: Fluids **27**, 684 (2008).

[37] Y. Shin, U. Rist, and E. Krämer, Stability of the laminar boundary-layer flow behind a roughness element, Exp. Fluids **56**, 11 (2015).

[38] M. S. Acarlar and C. R. Smith, A study of hairpin vortices in a laminar boundary layer, Part 1, Hairpin vortices generated by a hemisphere protuberance, J. Fluid Mech. **175**, 1 (1987).

[39] N. de Tullio, P. Paredes, N. D. Sandham, and V. Theofilis, Laminar-turbulent transition induced by discrete roughness element in a supersonic boundary layer, J. Fluid Mech. **735**, 613 (2013).

[40] A. Theiss, S. Hein, S. Ali, and R. Radespiel, Wake flow instability studies behind discrete roughness elements on a generic re-entry capsule, in *46th AIAA Fluid Dynamics Conference* (AIAA, AIAA Reston, USA, 2016).

[41] M. Bernardini, S. Pirozzoli, and P. Orlandi, Compressibility effects on roughness-induced boundary layer transition, Int. J. Heat Fluid Flow **35**, 45 (2012).

[42] J. A. Redford, N. D. Sandham, and G. T. Roberts, Compressibility effects on boundary-layer transition induced by an isolated roughness element, AIAA J. **48**, 2818 (2010).

[43] J. Loiseau, S. Cherubini, J. Robinet, and E. Leriche, Influence of the shape on the roughness-induced transition, Fluid Mech. Applications **107**, 123 (2015).

[44] D. K. Puckert and U. Rist, Experiments on critical Reynolds number and global instability in roughness-induced laminar-turbulent transition, J. Fluid Mech. **844**, 878 (2018).

[45] S. Cherubini, M. D. De Tullio, P. De Palma, and G. Pascazio, Transient growth in the flow past a three-dimensional smooth roughness element, J. Fluid Mech. **724**, 642 (2013).

[46] Q. Ye, F. F. Schrijer, and F. Scarano, Boundary layer transition mechanisms behind a micro-ramp, J. Fluid Mech. **793**, 132 (2016).

[47] M. A. Bucci, D. Puckert, C. Andriano, J. Loiseau, S. Cherubini, J. Robinet, and U. Rist, Roughness-induced transition by quasi-resonance of a varicose global mode, J. Fluid Mech. **836**, 167 (2018).

[48] D. Sipp and O. Marquet, Characterization of noise amplifiers with global singular modes: The case of the leading-edge flat-plate boundary layer, Theoret. Comput. Fluid Dynamics **27**, 617 (2013).

[49] L. Siconolfi, S. Camarri, and J. H. M. Fransson, Boundary layer stabilization using free-stream vortices, J. Fluid Mech. **764**, R2 (2015).

[50] X. Garnaud, L. Lesshafft, P. J. Schmid, and P. Huerre, The preferred mode of incompressible jets: Linear frequency response analysis, J. Fluid Mech. **716**, 189 (2013).

[51] E. Cowled, *The Effects of Surface Irregularities on Transition in the Laminar Boundary Layer* (Aeronautical Research Laboratories, Victoria, Australia, 1954).

[52] A. L. Braslow, Review of the effect of distributed surface roughness on boundary-layer transition, Tech. Rep., Advisory Group for Aeronautical Research and Development, Paris, France, 1960.

[53] P. F. Fischer, J. W. Lottes, and S. G. Kerkemeier, nek5000 web page, http://nek5000.mcs.anl.gov

[54] A. T. Patera, A spectral element method for fluid dynamics: Laminar flow in a channel expansion, J. Comput. Phys. **54**, 468 (1984).

[55] M. Deville, P. Fischer, and E. Mund, *High-Order Methods for Incompressible Fluid Flow* (Cambridge University Press, Cambridge, 2002).

[56] R. G. Jacobs and P. A. Durbin, Simulations of bypass transition, J. Fluid Mech. **428**, 185 (2001).

[57] P. Schlatter, Direct numerical simulation of laminar-turbulent transition in boundary layer subject to free-stream turbulence, Master's thesis, Royal Institute of Technology, Stockholm, 2001.

[58] P. J. Schmid, Dynamic mode decomposition of numerical and experimental data, J. Fluid Mech. **656**, 5 (2010).

[59] M. R. Jovanović, P. J. Schmid, and J. W. Nichols, Sparsity-promoting dynamic mode decomposition, Phys. Fluids **26**, 024103 (2014).

[60] B. O. Koopman, Hamiltonian systems and transformation in Hilbert space, Proc. Natl. Acad. Sci. USA **17**, 315 (1931).

[61] J. N. Kutz, S. L. Brunton, B. W. Brunton, and J. L. Proctor, *Dynamic Mode Decomposition: Data-Driven Modeling of Complex Systems* (Society for Industrial and Applied Mathematics, Philadelphia, USA, 2016).

[62] W. S. Edwards, L. S. Tuckerman, R. A. Friesner, and D. C. Sorensen, Krylov methods for the incompressible Navier-Stokes equations, J. Comput. Phys. **110**, 82 (1994).

[63] S. Bagheri, P. Schlatter, P. J. Schmid, and D. S. Henningson, Global stability of a jet in crossflow, J. Fluid Mech. **624**, 33 (2009).

[64] G. W. Stewart, A Krylov-Schur algorithm for large eigenproblems, SIAM J. Matrix Anal. Appl. **23**, 601 (2001).

[65] J.-C. Loiseau, M. A. Bucci, S. Cherubini, and J.-C. Robinet, Time-stepping and Krylov methods for large-scale instability problems, in *Computational Modelling of Bifurcations and Instabilities in Fluid Dynamics* (Springer, Berlin, 2019), pp. 33–73.

[66] V. Citro, P. Luchini, F. Giannetti, and F. Auteri, Efficient stabilization and acceleration of numerical simulation of fluid flows by residual recombination, J. Comput. Phys. **344**, 234 (2017).

[67] A. Monokrousos, E. Åkervik, L. Brandt, and D. S. Henningson, Global three-dimensional optimal disturbances in the Blasius boundary-layer flow using time-steppers, J. Fluid Mech. **650**, 181 (2010).

[68] D. K. Puckert, M. Dieterle, and U. Rist, Reduction of freestream turbulence at low velocities, Exp. Fluids **58**, 45 (2017).

[69] C. Cossu and L. Brandt, On Tollmien-Schlichting-like waves in streaky boundary layers, Eur. J. Mech. B: Fluids **23**, 815 (2004).

[70] I. Tani and H. Komoda, Boundary layer transition in the presence of streamwise vortices, J. Aerosp. Sci. **29**, 440 (1962).

[71] H. U. Meier and H.-P. Kreplin, Experimental investigation of the boundary layer transition and separation on a body of revolution, Zeitschrift fuer Flugwissenschaften und Weltraumforschung **4**, 65 (1980).

[72] P. Luchini, Reynolds-number-independent instability of the boundary layer over a flat surface: Optimal perturbations, J. Fluid Mech. **404**, 289 (2000).

[73] S. Cherubini, J.-C. Robinet, A. Bottaro, and P. De Palma, Optimal wave packets in a boundary layer and initial phases of a turbulent spot, J. Fluid Mech. **656**, 231 (2010).

[74] S. Albensoeder, H. Kuhlmann, and H. Rath, Three-dimensional centrifugal-flow instabilities in the lid-driven-cavity problem, Phys. Fluids **13**, 121 (2001).

[75] Q. Ye, F. F. J. Schrijer, and F. Scarano, Geometry effect of isolated roughness on boundary layer transition investigated by tomographic piv, Int. J. Heat Fluid Flow **61**, 31 (2016).

[76] J. Cohen, M. Karp, and V. Mehta, A minimal flow-elements model for the generation of packets of hairpin vortices in shear flows, J. Fluid Mech. **747**, 30 (2014).

[77] M. J. P. Hack and P. Moin, Coherent instability in wall-bounded shear, J. Fluid Mech. **844**, 917 (2018).

[78] M. Farano, S. Cherubini, J.-C. Robinet, and P. De Palma, Hairpin-like optimal perturbations in plane poiseuille flow, J. Fluid Mech. **775**, R2 (2015).

[79] R. J. Adrian, Hairpin vortex organization in wall turbulence, Phys. Fluids **19**, 041301 (2007).

[80] S. Shahinfar, J. H. M. Fransson, S. S. Sattarzadeh, and A. Talamelli, Scaling of streamwise boundary layer streaks and their ability to reduce skin-friction drag, J. Fluid Mech. **733**, 1 (2013).

[81] H. B. E. Kurz and M. J. Kloker, Mechanisms of flow tripping by discrete roughness elements in a swept-wing boundary layer, J. Fluid Mech. **796**, 158 (2016).

[82] M. Brynjell-Rahkola, N. Shahriari, P. Schlatter, A. Hanifi, and D. S. Henningson, Stability and sensitivity of a cross-flow-dominated Falkner-Skan-Cooke boundary layer with discrete surface roughness, J. Fluid Mech. **826**, 830 (2017).

[83] D. P. G. Foures, C. P. Caulfield, and P. J. Schmid, Localization of flow structures using ∞-norm optimization, J. Fluid Mech. **729**, 672 (2013).

[84] M. Farano, S. Cherubini, J.-C. Robinet, and P. De Palma, Optimal bursts in turbulent channel flow, J. Fluid Mech. **817**, 35 (2017).

[85] M. Carini, F. Giannetti, and F. Auteri, On the origin of the flip–flop instability of two side-by-side cylinder wakes, J. Fluid Mech. **742**, 552 (2014).